From superdeformation to extreme deformation and clusterization in the $N \approx Z$ nuclei of the $A \approx 40$ mass region

D. Ray and A. V. Afanasjev
Department of Physics and Astronomy, Mississippi State University, Mississippi 39762, USA
(Received 20 April 2016; revised manuscript received 4 June 2016; published 14 July 2016)

A systematic search for extremely deformed structures in the $N \approx Z$ nuclei of the $A \approx 40$ mass region has been performed for the first time in the framework of covariant density functional theory. At spin zero such structures are located at high excitation energies, which prevents their experimental observation. The rotation acts as a tool to bring these exotic shapes to the yrast line or its vicinity so that their observation could become possible with future generation of γ-tracking (or similar) detectors such as GRETA and AGATA. The major physical observables of such structures (such as transition quadrupole moments, as well as kinematic and dynamic moments of inertia), the underlying single-particle structure and the spins at which they become yrast or near yrast, are defined. The search for the fingerprints of clusterization and molecular structures is performed and the configurations with such features are discussed. The best candidates for observation of extremely deformed structures are identified. For several nuclei in this study (such as ^{36}Ar), the addition of several spin units above the currently measured maximum spin of $16\hbar$ will inevitably trigger the transition to hyper- and megadeformed nuclear shapes.

DOI: 10.1103/PhysRevC.94.014310

I. INTRODUCTION

There is considerable interest in the study of cluster structures and extremely deformed shapes in light nuclei [1–10]. Many of these structures are described in terms of clusters, the simplest one being the α particle [2,3]. Providing a unique insight into the cluster dynamics inside a nucleus, the initial assumptions about clusters represent a limitation of this type of model. Note also that many shell-model configurations are beyond the reach of the cluster models. It is also important to remember that the cluster description does not correspond to clearly separated α particles, but generates the mean-field states largely by antisymmetrization [3]. In addition, the studies of molecular structures, which appear in many extremely deformed configurations, have gained considerable interest [2,7,11].

In recent years, the investigations of exotic cluster configurations have been undertaken also in the density functional theory (DFT). The advantage of the DFT framework is the fact that it does not assume the existence of cluster structures; the formation of cluster structures proceeds from microscopic single-nucleon degrees of freedom via many-body correlations [6,12]. As a result, the DFT framework allows simultaneous treatment of cluster and mean-field-type states [5,6,12–14]. It is important to mention that covariant (relativistic) energy density functionals (CEDFs) show more pronounced clusterization of the density distribution than nonrelativistic ones because of deeper single-nucleon potentials [6].

Let us mention some recent studies of cluster and extremely deformed structures in the DFT framework. The clustering phenomenon in light stable and exotic nuclei was studied within the relativistic mean-field (RMF) approach in Ref. [15] and within the Hartree-Fock (HF) approach based on the Skyrme energy density functionals (EDFs) in Ref. [5]. Linear chain configurations of four α clusters in ^{16}O and the relationship between the stability of such states and angular momentum were investigated using the Skyrme cranked HF method in Ref. [16] and cranked RMF (CRMF) in Ref. [14]. This is an example of the "rod-shaped" nucleus. Another case of such structures is a linear chain of three α clusters, suggested about 60 yr ago [17]; it was recently studied in the CRMF theory in Ref. [8]. This exotic structure ("Hoyle" state) plays a crucial role in the synthesis of ^{12}C from three ^{4}He nuclei in stars [18]. The stability of rod-shaped structures in highly excited states of ^{24}Mg was studied in Ref. [9] in cranked Skyrme HF calculations.

The difficulty in investigating cluster and extremely deformed states is that they are generally unbound and lie at high excitation energies at low spins [2,10]. Moreover, they are formed either on the shoulder or in very shallow minima of potential energy surfaces [12,19]; thus, they are inherently unstable at low spin. The high density of nucleonic configurations at these energies and possible mixing among them is another factor hindering their observation with current and future generations of experimental facilities. Moreover, obtaining unambiguous evidence for clustering (such as a transition strengths between different states and the structure of the wave function) is equally challenging and frequently ambiguous from experimental point of view. In addition, the mechanisms of the reactions used in experimental studies frequently favor the population of yrast or near-yrast states [10].

The rotation of the nucleus could help to overcome these problems in experimental observation of extremely deformed structures. Two factors are contributing to that. First, very large deformation configurations [such as superdeformed (SD), hyperdeformed (HD), and megadeformed (MD) ones] are favored by rotation at high spins (see, for example, the discussion in Refs. [19,21]). Second, normal- and highly deformed configurations, which are forming yrast or near-yrast structures at low and medium spins, have limited angular momentum content. As a consequence, only extreme deformation structures (SD, HD, or MD) could be populated above some specific spin values in the nuclei of interest.

Our systematic search for extremely deformed configurations is focused on the $N = Z$ and $N = Z + 2$ even-even S ($Z = 16$), Ar ($Z = 18$), Ca ($Z = 40$), Ti ($Z = 42$), Cr ($Z = 44$) (and also on $N = Z + 4$ ^{44}Ca), and odd-odd $N = Z = 21$ ^{42}Sc nuclei. The selection of the nuclei is motivated by several factors. First, the ^{40}Ca nucleus is a centerpiece of this study because of its highly unusual features. This is a doubly magic spherical nucleus (in the ground state) in which normal- and superdeformed configurations based on the four-particle–four-hole (4p-4h) and eight-particle–eight-hole (8p-8h) excitations, respectively, are observed at low excitation energies (Ref. [22]). The two-dimensional α-cluster model predicts very exotic and highly deformed configurations in this nucleus [23]. Second, in this mass region the superdeformation has already been observed in the ^{40}Ca [22,24], ^{36}Ar [25,26], ^{35}Cl [27], ^{40}Ar [28], and probably ^{28}Si [29] nuclei. Moreover, the SD bands have been seen up to very high spin of $I = 16\hbar$ in some of these nuclei. This is quite an important fact because, according to the results obtained in the present paper, further modest increase of the spin could lead to the population of extremely deformed structures in some of the nuclei. When populated, such structures could be observed with the next generation of the γ-tracking detectors such as GRETA and AGATA. In addition, the resonance observed at $I \approx 36\hbar$ in the ^{24}Mg $+^{24}$Mg reaction strongly supports the HD shape for a compound ^{48}Cr nucleus formed in this reaction [30]. Moreover, the analysis of light particle energy spectra and angular correlations in the framework of the statistical model indicates the onset of large deformations at high spin in ^{44}Ti [31]. Third, in experiment the high-spin structures in this mass region are better populated in the $N \approx Z$ nuclei. Note also that at present high-spin studies are quite active in this mass region [30,32–35].

There are theoretical studies of deformed structures in these nuclei but they either focus on SD structures at high spin or are limited to a shape coexistence at low spin. For example, positive-parity states of ^{40}Ca were studied in Ref. [4] using antisymmetrized molecular dynamics (AMD) and the generator coordinate method (GCM); this is basically the α-clustering model. The coexistence of low-spin normal- and superdeformed states in ^{32}S, ^{36}Ar, ^{38}Ar, and ^{40}Ca has been studied in the GCM based on the Skyrme SLy6 functional in Ref. [36]. The SD and HD rotational bands in the $N = Z$ S, Ar, Ca, Ti, and Cr nuclei have also been studied in the cranked Hartree-Fock (CHF) approach based on the Skyrme forces in Refs. [37,38]. Special attention has been paid to the SD structures in ^{32}S, which were studied in detail in the CHF frameworks based on Skyrme [37,39] and Gogny [40] forces and CRMF theory [41]. Exotic and highly deformed α-cluster configurations have been predicted long time ago in the two-dimensional α-cluster model in $4N$ nuclei from ^{12}C to ^{44}Ti in Ref. [23]. The investigation of superdeformation and clustering in these nuclei still remains an active field of research within the cluster models (see Refs. [1,3,4,7,42]).

There are several goals behind this study. First, it is imperative to understand at which spins extremely deformed configurations are expected to become yrast (or come close to the vicinity of the yrast line) and to find the best candidates for experimental studies of such structures. This requires detailed knowledge of terminating configurations up to their terminating states because they form the yrast line at low and medium spins. However, the tracing of terminating configurations from low spin up to their terminating states is nontrivial problem in density functional theories (see Sec. 8 in Ref. [43] and Ref. [44]). To our knowledge, such calculations have been done so far only in few nuclei: ^{20}Ne (in the cranked Skyrme HF [45] and CRMF [46,47] frameworks), ^{48}Cr (in the HFB framework with Gogny forces [48]), and ^{109}Sb (in the CRMF framework [43]). Note also that in ^{109}Sb they fail to reach the terminating state. With appropriate improvements in the CRMF computer code we are able to perform such calculations for the majority of the configurations forming the yrast line at low and medium spins. Second, the basic properties (such as transition quadrupole moments and dynamic and kinematic moments of inertia) of the configurations of interest, which could be compared in the future with experimental data, are predicted. Third, we search for the fingerprints of the clusterization and molecular structures via a detailed analysis of the density distributions of the configurations under study.

The paper is organized as follows. Section II describes the details of the solutions of the cranked relativistic mean-field equations. Detailed analysis of the structure of rotational spectra of ^{40}Ca and ^{42}Sc is presented in Secs. III and IV, respectively. Special attention is paid to the dependence of density distributions on the configuration. The general features of rotational spectra along the yrast line are discussed in Sec. V. Section VI is devoted to the discussion of the appearance of super-, hyper-, and megadeformed configurations along the yrast line of the ^{32,34}S, ^{36,38}Ar, ^{42,44}Ca, ^{44,46}Ti, and ^{48,50}Cr nuclei and their properties. The configurations which reveal the fingerprints of clusterization and molecular structures in their density distributions are discussed in Sec. VII. The kinematic and dynamic moments of inertia of selected SD, HD, and MD configurations and their evolution with proton and neutron numbers and rotational frequency are considered in Sec. VIII. Finally, Sec. IX summarizes the results of our work.

II. THE DETAILS OF THE THEORETICAL CALCULATIONS

In the RMF theory the nucleus is described as a system of pointlike nucleons, Dirac spinors, coupled to mesons and to the photons [43,49,50]. The nucleons interact by the exchange of several mesons, namely a scalar meson σ and three vector particles, ω, ρ, and the photon. The CRMF theory [46,51,52] is the extension of the RMF theory to the rotating frame in one-dimensional cranking approximation. It represents the realization of covariant density functional theory (CDFT) for rotating nuclei with no pairing correlations [43]. It has successfully been tested in a systematic way on the properties of different types of rotational bands in the regime of weak pairing such as normal-deformed [53] and superdeformed [52,54], as well as smooth terminating bands [43] and the bands at the extremes of angular momentum [55].

The formalism and the applications of the CRMF theory to the description of rotating nuclei have recently been reviewed in Ref. [56] (see also Refs. [43,57]). A clear advantage of the CRMF framework for the description of rotating nuclei

is the treatment of time-odd mean fields which are uniquely defined via the Lorentz covariance [58]; note that these fields substantially affect the properties of rotating nuclei [47,59]. Because the details of the CRMF framework could be found in earlier publications (Refs. [19,46,51,52]), we focus here on the features typical for the present study.

The pairing correlations are neglected in the present calculations. There are several reasons behind this choice. First, it is well known that pairing correlations are quenched by rotation (Coriolis antipairing effect) [60,61]. The presence of substantial shell gaps also leads to a quenching of pairing correlations [62]. Another mechanism of pairing quenching is the blocking effect, which is active in many nucleonic configurations [60]. In a given configuration, the pairing is also very weak at the spins close to band termination [20]. Moreover, the pairing drastically decreases after paired band crossings in the proton and neutron subsystems [53]; at these spins the results of the calculations with and without pairing are very similar.

Second, the calculations for blocked configurations within the cranked relativistic Hartree-Bogoliubov (CRHB) framework [63] are frequently numerically unstable [57]. This is a common problem for self-consistent Hartree-Bogoliubov and Hartree-Fock-Bogoliubov calculations which appear in both relativistic and nonrelativistic frameworks [64]. On the contrary, these problems are much less frequent in unpaired CRMF calculations (see Ref. [19]). Even then it is not always possible to trace the configuration in the desired spin range. This typically takes place when (i) the local minimum is not deep enough for the solution (unconstrained in quadrupole moments) to stay in it during convergence process and (ii) occupied and unoccupied single-particle orbitals with the same quantum numbers come close in energy and start to interact.

Based on previous experience in ^{40}Ca [22], ^{48}Cr [20], and somewhat heavier $N \approx Z$ $A = 58$–80 nuclei [53,54], we estimate that the pairing becomes quite small and thus is not very important above $I \approx 10\hbar$ in the nuclei of interest. This is exactly the spin range on which the current study is focused. Note also that the comparison of the CRHB and CRMF results for a few configurations in ^{40}Ca presented at the end of Sec. III supports this conclusion.

In the current study, we restrict ourselves to reflection symmetric shapes because previous calculations in the cranked Hartree-Fock approach with Skyrme forces [38] showed that odd-multipole (octupole, . . .) deformations play a very limited role in extremely deformed configurations of the mass region under study.

The CRMF equations are solved in the basis of an anisotropic three-dimensional harmonic oscillator in Cartesian coordinates characterized by the deformation parameters β_0 and γ and oscillator frequency $\hbar\omega_0 = 41A^{1/3}$ MeV; for details, see Refs. [46,52]. The truncation of basis is performed in such a way that all states belonging to the major shells up to $N_F = 14$ fermionic shells for the Dirac spinors and up to $N_B = 20$ bosonic shells for the meson fields are taken into account. This truncation scheme provides sufficient numerical accuracy (see Ref. [19] for details).

The CRMF calculations have been performed with the NL3* functional [65], which is a state-of-the-art functional for the nonlinear meson-nucleon coupling model [66]. It is globally tested for ground-state observables in even-even nuclei [66] and systematically tested for physical observables related to excited states in heavy nuclei [57,67,68]. The CRMF and CRHB calculations with the NL3* CEDF provide a very successful description of different types of rotational bands [55,57,65] at both low and high spins.

The quadrupole deformation β_2 is defined in self-consistent calculations from calculated quadrupole moments using the simple relation [69–71]

$$\beta_2 = \frac{1}{XR^2}\sqrt{\frac{5\pi}{9}}\,Q_0^X, \tag{1}$$

where $R = 1.2A^{1/3}$ fm is the radius and Q_0^X is a quadrupole moment of the Xth (sub)system expressed in fm^2. Here X refers either to proton ($X = Z$) or neutron ($X = N$) subsystem or represents total nuclear system ($X = A$). However, this expression neglects the higher powers of β_2 and higher multipolarity deformations β_4, β_6, . . . [72], which have an important role at very large deformations.

Because the definition of the deformation is model dependent [72] and deformation parameters are not experimentally measurable quantities, we prefer to use transition quadrupole moment Q_t for the description of deformation properties of the SD, HD, and MD bands. This is an experimentally measurable quantity and thus in the future our predictions can be directly compared with the experimental results. The deformation properties of the yrast SD band in ^{40}Ca [22] are used as a reference. The measured transition quadrupole moment of this band is $Q_t^{\rm exp} = 1.8^{+0.35}_{-0.29}\,e$b [22]. Note that the CRMF calculations with the NL3* functional come close to experiment only slightly overestimating an experimental value (see Fig. 5 below). Thus, we use $Q_t^{\rm exp} = 1.8\,e$b in ^{40}Ca as a reference point. Note that the SD band in ^{40}Ca is the most deformed SD band among observed SD bands in this mass region.

Using this value we introduce the normalized transition quadrupole moment $Q_t^{\rm norm}(Z,A)$ in the (Z,A) system,

$$Q_t^{\rm norm}(Z,A) = \frac{ZA^{2/3}}{129.96}\,e\text{b}. \tag{2}$$

This is similar to what has been done in Ref. [19] in the analysis of the HD configurations in the medium-mass region. This equation is based on the ratio $Q_t^{\rm norm}(Z,A)/Q_t(^{40}\text{Ca})$ calculated using Eq. (1) under the assumption that the β_2 values in the (Z,A) system and in ^{40}Ca are the same.

The band will be described as HD if its calculated Q_t value exceeds $Q_t^{\rm norm}(Z,A)$ by approximately 50%. This definition of HD is similar to the one employed in Ref. [19]. Following the suggestion of Ref. [21], we describe even more deformed bands as megadeformed. The band is classified as MD when its calculated Q_t value is approximately twice that of $Q_t^{\rm norm}(Z,A)$ or higher.

Single-particle orbitals are labeled by $\Omega[Nn_z\Lambda](r = \pm i)$. $\Omega[Nn_z\Lambda]$ are the asymptotic quantum numbers (Nilsson quantum numbers) of the dominant component of the wave function at $\Omega_x = 0.0$ MeV and r is the signature of the orbital.

Because the pairing correlations are neglected, the intrinsic structure of the configurations of interest can be described by means of the dominant single-particle components of the intruder/hyperintruder/megaintruder states occupied. Thus, the calculated configurations will be labeled by shorthand $[n_1(n_2)(n_3), p_1(p_2)(p_3)]$ labels, where n_1, n_2, and n_3 are the number of neutrons in the $N = 3$, 4, and 5 intruder/hyperintruder/megaintruder orbitals and p_1, p_2, and p_3 are the number of protons in the $N = 3$, 4, and 5 intruder/hyperintruder/megaintruder orbitals. The $N = 5$ megaintruder orbitals are not occupied in the HD configurations. As a consequence, the labels n_3 and p_3 are omitted in the labeling of such configurations. Moreover, the $N = 4$ and $N = 5$ orbitals are not occupied in the SD configurations. So, in those configurations the n_2, n_3 and p_2, p_3 labels are omitted. An additional letter *(a,b,c,...)* at the end of the shorthand label is used to distinguish the configurations that have the same occupation of the intruder/hyperintruder/megaintruder orbitals (the same $[n_1(n_2)(n_3), p_1(p_2)(p_3)]$ label) but differ in the occupation of nonintruder orbitals.

III. THE ^{40}Ca NUCLEUS

^{40}Ca is a doubly magic spherical nucleus with 20 neutrons and 20 protons. The three lowest shells with $N = 0$, 1, and 2 are occupied in its spherical ground state with $I = 0^+$. Higher spin states are formed by particle-hole excitations from the $N = 2$ shell into $f_{7/2}(N = 3)$ subshell across the respective $Z = 20$ and $N = 20$ spherical shell gaps. This leads to a formation of complicated high-spin level scheme which includes spherical states and deformed, terminating, and superdeformed rotational structures [22,24,73]. In experiment, they extend up to spin $I = 16^+$.

The results of the CRMF calculations for deformed configurations forming the yrast line are shown in Fig. 1. Different colors are used to indicate different classes of the bands. Note that low-spin spherical solutions are not shown here because we are interested in high-spin behavior of this nucleus.

The lowest deformed configuration [1,1] is based on simultaneous excitations of proton and neutron from the $d_{3/2}$ spherical subshell into the $f_{7/2}$ subshell across the $Z = 20$ and $N = 20$ spherical gaps. It has small quadrupole deformation of $\beta_2 \approx 0.16$ and $\gamma \approx -24^\circ$ at $I = 4\hbar$ and terminates at $I = 10^+$ in a terminating state with the structure $\pi(f_{7/2})^1_{3.5}(d_{3/2})^{-1}_{1.5} \otimes \nu(f_{7/2})^1_{3.5}(d_{3/2})^{-1}_{1.5}$ and near-spherical shape. Additional excitations of the proton and neutron across the $Z = 20$ and $N = 20$ spherical gaps lead to a more deformed [2,2] configuration, which has $\beta_2 \approx 0.32$ and $\gamma \approx -30^\circ$ at $I = 10\hbar$. It is expected to terminate at $I_{\max} = 20\hbar$ with the terminating state built at high energy cost and located high above the yrast line. However, we were not able to trace this configuration up to termination in the calculations. The next excitations of proton and neutron across the $Z = 20$ and $N = 20$ spherical gaps lead to even more deformed [3,3] configurations, which are located close to each other up to spin $I = 16\hbar$ (see Fig. 1). The configuration that terminates at spin $I = 18\hbar$ is located in positive γ minimum of potential energy surfaces and has $\beta_2 \approx 0.47$ and $\gamma \approx 21^\circ$ at $I = 12\hbar$. The structure of terminating state is $\pi(f_{7/2})^3_{7.5}(d_{3/2})^{-3}_{1.5} \otimes \nu(f_{7/2})^3_{7.5}(d_{3/2})^{-3}_{1.5}$. Another [3,3] configuration is located in the negative γ minimum of potential energy surfaces and is expected to terminate at $I = 24^+$. Similar to the [2,2] configuration, we were not able to trace it up to a terminating state, which is expected to be located high above the yrast line.

Subsequent particle-hole excitations lead to an increase of the deformation of the configurations, resulting in the formation of superdeformed rotational bands. Note that the bands with such deformation do not terminate in the single-particle terminating states (see Sec. 2.5 of Ref. [20]). The yrast SD configuration [4,4] is characterized by large SD shell gap at particle number 20 in both the proton and the neutron subsystems (Fig. 2). All single-particle states below these gaps are occupied in the [4,4] configuration. Note that a part of the Coulomb shift in energy the proton Routhian diagram is similar to the neutron one shown in Fig. 2. The [4,4] configuration is only yrast at $I = 22\hbar$; it is located above the yrast line at lower spin, in agreement with the experiment [22]. The accuracy of the description of the experimental data (dynamic and kinematic moments of inertia, transition quadrupole moments) is similar to that obtained with the NL1 CEDF; the results obtained with this functional are compared with experiment in Ref. [22].

Starting from the yrast SD configuration [4,4], there are two ways to build excited configurations. The first one is by exciting particles from the $3/2[321](r = \pm i)$ orbitals into the $1/2[200](r = \pm i)$ orbitals; they are shown as the S1–S4 excitations in Fig. 2. The combination of proton and neutron excitations of this type leads to the [3,3] configurations. If the proton (neutron) excitations of this type are combined with the neutron (proton) configuration of the yrast SD band, the [3,4] and [4,3] configurations are created. These configurations are excited with respect to the yrast [4,4] SD configuration; some of them are shown by red lines in Fig. 1. Note that, owing to the similarity of the proton and neutron Routhian diagrams, some of these excited configurations are degenerated (or nearly degenerated) in energy. In addition, we show only some of highly excited SD configurations for the sake of clarity. An important feature is quite large energy gap between the yrast [4,4] and lowest excited [3,3]d SD configurations. Such a situation favors the observation of the yrast SD band because the feeding intensity is concentrated on it (see discussion in Refs. [19,74]).

Alternatively, one can excite the particle from either the $5/2[202](r = -i)$ or the $5/2[202](r = +i)$ orbital to the lowest-in-energy hyperintruder $1/2[440](r = -i)$ orbital emerging from hyperintruder $N = 4$ shell; the occupation corresponding to such a configuration is shown on left side of Fig. 3. The combination of the proton and neutron excitations of this kind leads to fourfold degenerate [41,41] HD configurations. This degeneracy is attributable to very small signature splitting of the configurations built on opposite signatures of the $5/2[202]$ orbitals and the combination of proton and neutron configurations of this kind.

At first glance, this statement is in contradiction with Fig. 3, where there is a substantial energy splitting between the $r = -i$ and the $r = +i$ branches of the $5/2[202]$ orbital, which are almost parallel in rotational frequency. This feature is the consequence of nonpairwise occupation of the opposite

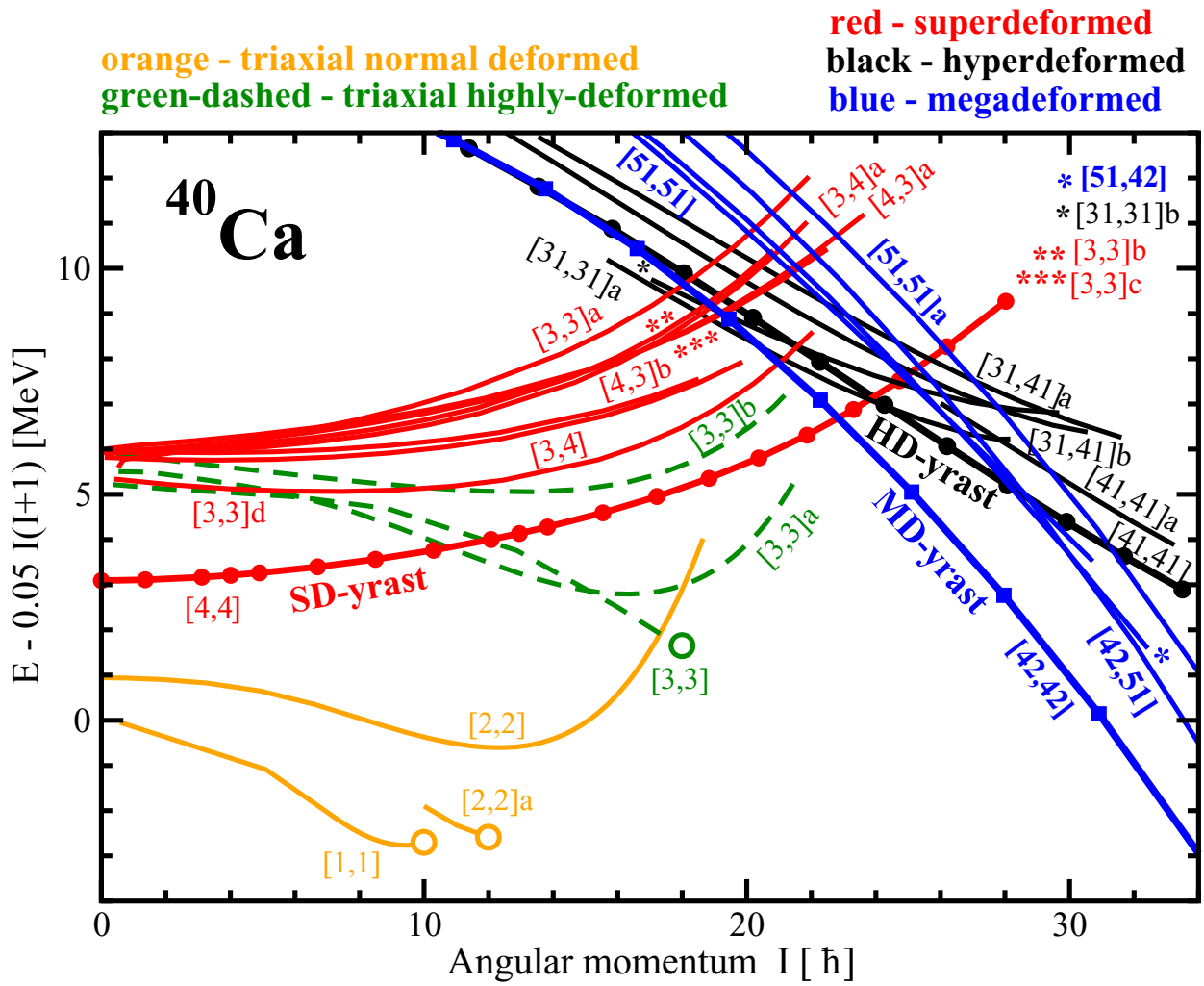

FIG. 1. Energies of the calculated configurations in ^{40}Ca relative to a smooth liquid drop reference $AI(I+1)$, with the inertia parameter $A = 0.05$. This way of the presentation of the results has clear advantages as compared with the energy versus spin plots; see Sec. 4.1 in Ref. [20] for details. Different types of configurations are shown by different types of lines. The SD, HD, and MD configurations, which are yrast in respective deformation minima, are shown by thick lines with symbols.

signatures of some orbitals, which leads to the presence of nucleonic currents at rotational frequency $\Omega_x = 0.0$ MeV (see Sec. IV A in Ref. [58]). The occupied orbital is always more bound than its unoccupied time-reversal counterpart. So the change of the signature of occupied 5/2[202] state (from $r = -i$ in Fig. 3 to $r = +i$) will only inverse the relative positions of both signatures of this orbital so that the total energy of the configurations built on the holes in the 5/2[202]($r = -i$) and 5/2[202]($r = +i$) orbitals will be almost the same.

The [41,41] configurations are the lowest in energy among the HD configurations at spins above $I = 24\hbar$ (Fig. 1). The excited HD configurations [31,31]a and [31,31]b (Fig. 1) are formed as the combination of the H1 and H2 excitations (shown in Fig. 3) in the proton and neutron subsystems. The [31,41]a and [31,41]b configurations are based on the H1 and H2 excitations in the neutron subsystem and the proton configuration of the yrast [41,41] HD configuration. The [41,31]a and [41,31]b configurations (not shown in Fig. 1), based on the H1 and H2 excitations in the proton subsystem and the neutron configuration of the yrast [41,41] HD configuration, are located at the energies that are similar to the ones of the [31,41]a and [31,41]b configurations.

The HD configurations never become yrast in ^{40}Ca. However, such configurations compete with megadeformed ones for yrast status in neigboring nuclei (see, for example, Secs. IV and VI A). That was a reason for a quite detailed discussion of their structure.

The additional occupation of the $N = 4$ proton and neutron orbitals leads to the [42,42] MD configuration which is yrast at spin above $I = 23\hbar$ (Fig. 1). It is characterized by large (around 3 MeV) MD $Z = 20$ and $N = 20$ shell gaps (Fig. 4). Thus, this configuration can be considered as doubly magic megadeformed configuration. Indeed, excited MD configurations (such as [42,51], [51,51], [51,42], etc.) are located at excitation energy of more than 2 MeV with respect to the yrast MD configuration (Fig. 1). The fact that the yrast MD configuration [42,42] is separated from the excited configura-

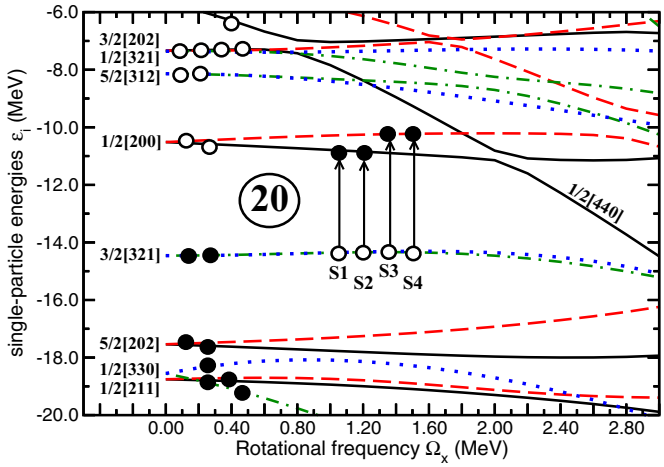

FIG. 2. Neutron single-particle energies (Routhians) in the self-consistent rotating potential as a function of the rotational frequency Ω_x. They are given along the deformation path of the yrast SD configuration in ^{40}Ca. Long-dashed, solid, dot-dashed, and dotted lines indicate $(\pi = +, r = +i)$, $(\pi = +, r = -i)$, $(\pi = -, r = +i)$, and $(\pi = -, r = -i)$ orbitals, respectively. At $\Omega_x = 0.0$ MeV, the single-particle orbitals are labeled by the asymptotic quantum numbers $[Nn_z\Lambda]\Omega$ (Nilsson quantum numbers) of the dominant component of the wave function. Solid (open) circles indicate the orbitals occupied (emptied). The arrows indicate the particle-hole excitations leading to excited SD configurations; for these configurations only the changes (as compared with yrast SD configuration) in the occupation of the orbitals are indicated in the figure.

tions by a such large energy gap should make its observation in experiment easier. This is because of the concentration of feeding intensity on the yrast MD configuration in such a situation (see discussion in Refs. [19,74]).

Calculated transition quadrupole moments Q_t and γ deformations of the normal- and highly deformed triaxial, SD, HD, and MD configurations are shown in Figs. 5, 6, and 7. The configurations which are yrast in local deformation

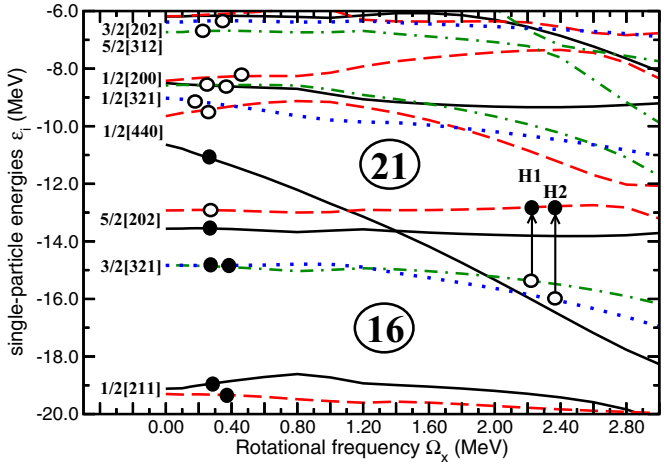

FIG. 3. The same as Fig. 2, but along the deformation path of the yrast HD configuration in ^{40}Ca. The arrows indicate the particle-hole excitations leading to excited HD configurations.

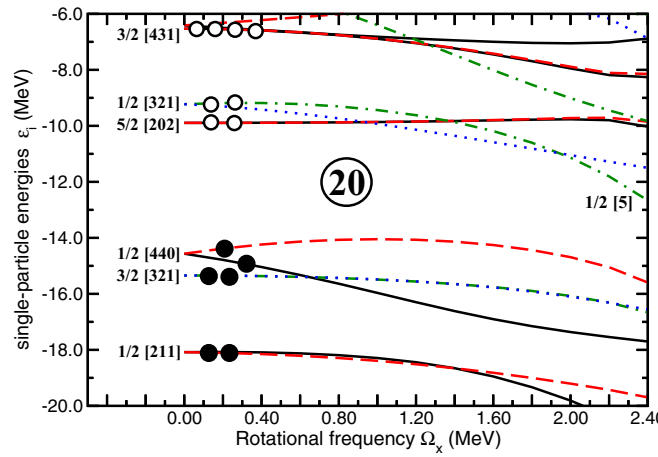

FIG. 4. The same as Fig. 2, but along the deformation path of the yrast MD [42,42] configuration in ^{40}Ca.

minimum, namely, SD [4,4], HD [41,41], and MD [42,42], have the largest transition quadrupole moment among the calculated SD, HD, and MD configurations, respectively. This is because particle-hole excitations leading to excited configurations reduce the number of occupied deformation driving orbitals.

Note that most of the calculated SD configurations have $\gamma \approx -12^\circ$. The only exception is the unusual [31,31]a configuration, which has large positive γ deformation rapidly increasing with spin. It has some similarities with the HD configurations. First, it involves the $N = 4$ proton and neutron. Second, its slope in the E-$E_{\rm RLD}$ plot is similar to the one of the HD configurations (see Fig. 1). However, it has substantially smaller Q_t values than the HD configurations.

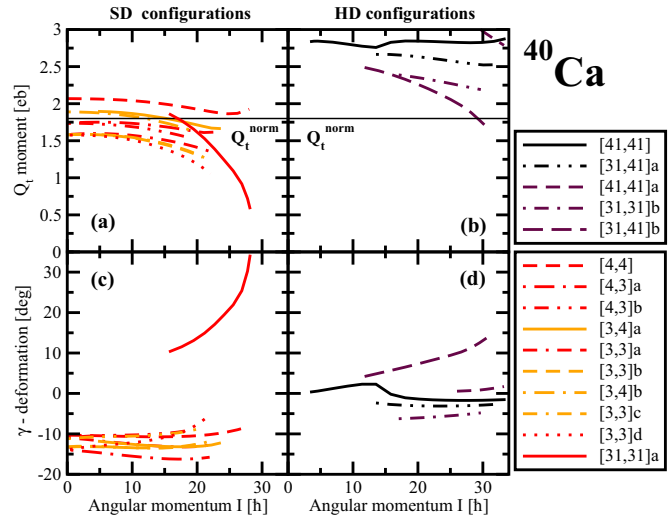

FIG. 5. Calculated transition quadrupole moments Q_t and γ deformations of the yrast and excited SD and HD configurations in ^{40}Ca. The colors of the lines for different types of configurations roughly correspond to those used in Fig. 1. Red and orange (black and dark brown) are used for the SD (HD) configurations.

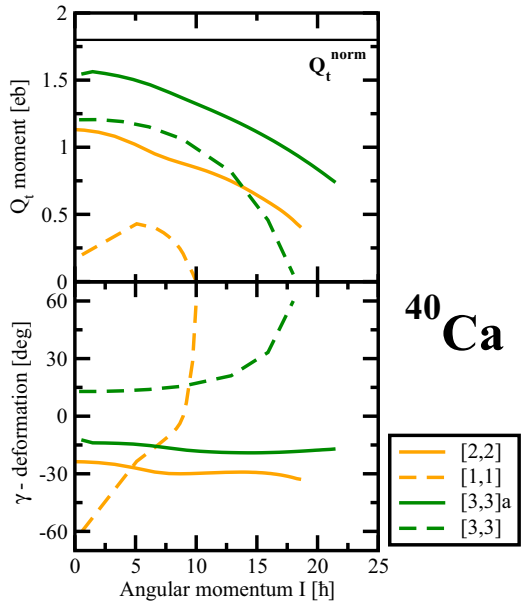

FIG. 6. The same as Fig. 5, but for the normal- and highly deformed triaxial configurations in ^{40}Ca.

While the calculated Q_t and γ values cluster for the SD configurations [Figs. 5(a) and 5(c)], they are scattered for the HD configurations [Figs. 5(b) and 5(d)]. This suggests that the potential energy surfaces are much softer in the HD minimum than in the SD one. Indeed, in the HD minimum a single particle-hole excitation induces much larger changes in the Q_t and γ values than in the SD one. On the contrary, the MD configurations show the clusterization of the calculated Q_t and γ values, which is similar to the one observed in the SD minimum (Fig. 7).

The most deformed HD configuration [41,41] has Q_t values that are by roughly 40% larger than the ones for most deformed

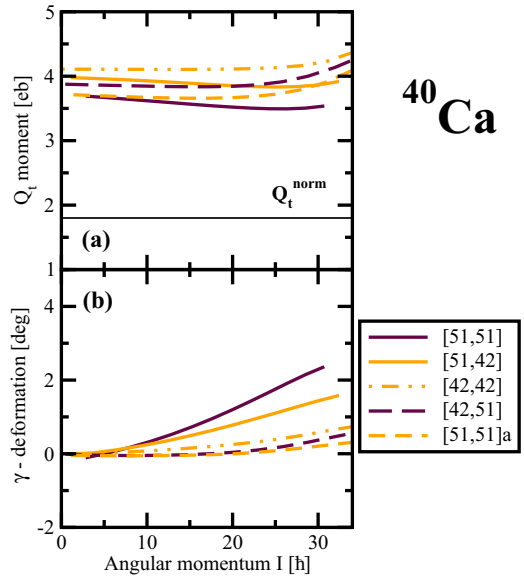

FIG. 7. The same as Fig. 5, but for the MD configurations in ^{40}Ca.

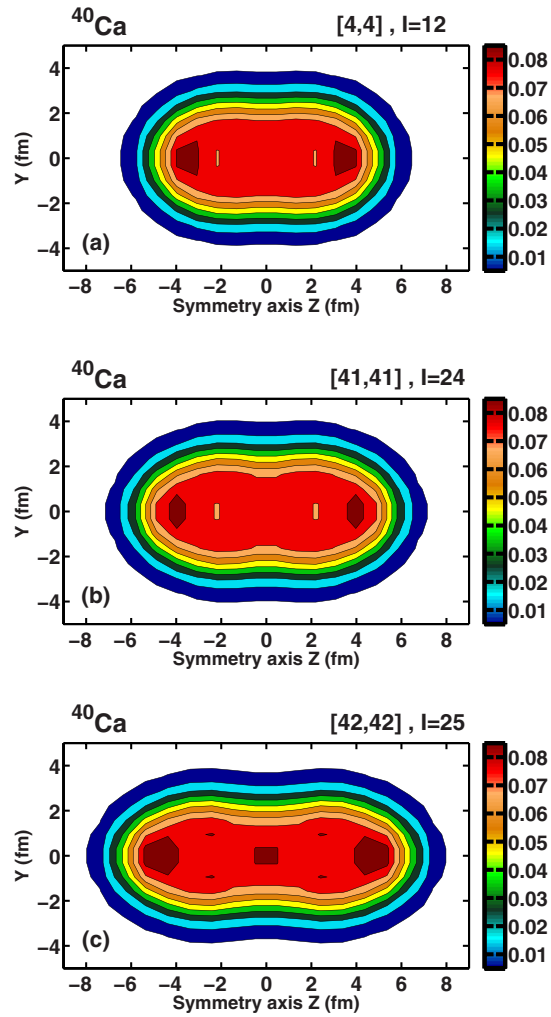

FIG. 8. The self-consistent proton density $\rho_p(y,z)$ as a function of y and z coordinates for the indicated configurations in ^{40}Ca at specified spin values. The equidensity lines are shown in steps of 0.01 fm^{-3} starting from $\rho_p(y,z) = 0.01$ fm^{-3}.

SD configuration [4,4)] [Figs. 5(a) and 5(c)]. Yrast MD configuration [42,42] has Q_t values that are larger by roughly 45% and 105% than the ones for most deformed HD and SD configurations [compare Figs. 7(a) and 5(a) and 5(c)].

The self-consistent proton densities of the yrast SD, HD, and MD configurations are shown in Fig. 8 at indicated spin values. The stretching of nuclear shape is definitely more pronounced in the HD [41,41] and especially in the MD [42,42] configurations. Indeed, the semimajor-to-semiminor axis ratio is 2.05, 2.27, and 2.9 for the densities of the SD [4,4], HD [41,41], and MD [42,42] configurations, respectively. Note that the changes in the semiaxis ratio on going from one type of configuration to another are substantially smaller than relevant changes in the Q_t values discussed above. The densities of the [41,41] HD configuration show some indications of the development of neck and these indications become much more pronounced in the MD [42,42] configuration.

Figure 9 compares the results of the calculations with and without pairing for few selected configurations in ^{40}Ca.

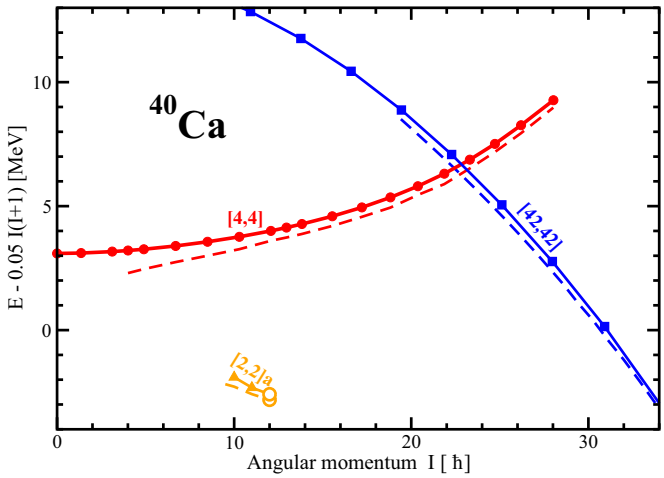

FIG. 9. The comparison of the results of the calculations with and without pairing for the configurations of ^{40}Ca that do not require blocking procedure in the CRHB calculations. The results of the calculations without pairing are shown by solid lines with symbols. The results for paired analogs of unpaired configurations are shown by dashed lines of the same color.

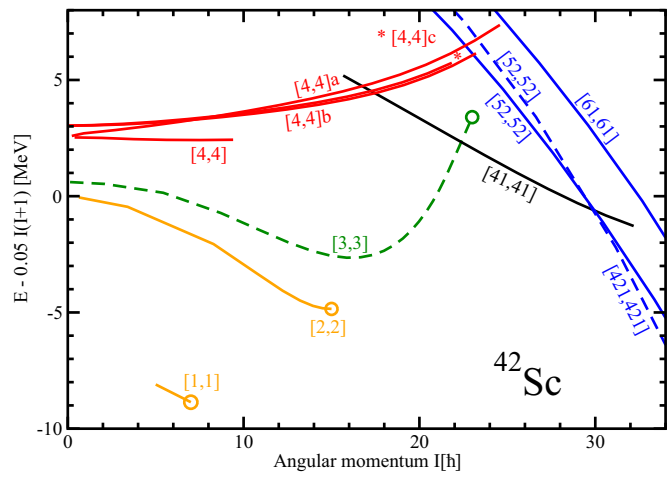

FIG. 10. The same as Fig. 1, but for ^{42}Sc.

The calculations with pairing are performed in the CRHB framework of Ref. [63]. In these calculations the Lipkin-Nogami method is employed for an approximate particle number projection and the Gogny D1S force is used in pairing channel. The presence of pairing correlations leads to an additional binding. However, above $I = 10\hbar$ this additional binding is rather modest (around 0.5 MeV or less) and it is similar for different calculated configurations. As a result, the general structure of the calculated configurations in the E-$E_{\rm RLD}$ plot above this spin is only weakly affected by the presence of pairing. A similar effect has already been seen in the case of ^{72}Kr (Ref. [75]).

Note that among a large number of the configurations obtained in unpaired calculations and presented in Fig. 1 only these three configurations (terminating [2,2]a, superdeformed [4,4], and hyperdeformed [42,42]), in which signature partner orbitals are pairwise occupied (see Figs. 2 and 4), can be calculated in the CRHB framework without a blocking procedure. Particle-hole excitations leading to excited configurations remove pairwise occupation of the signature partner orbitals. As a result, the blocking procedure has to be employed for the calculation of such configurations in the CRHB framework. For example, the blocking of two particles is needed if the configuration label contains at least one odd number in either proton or neutron subsystem. If the configuration label contains an odd number in both proton and neutron subsystems, then the blocking of four particles (two in proton subsystem and two in neutron subsystem) is needed. Such calculations are inherently unstable [57,76]. However, the blocking leads to an additional reduction of the impact of pairing correlations on physical observables (see Ref. [57]). As a result, an even smaller effect of pairing (as compared with the one shown in Fig. 9) is expected on binding energies of the configurations of Fig. 1 not shown in Fig. 9.

IV. ^{42}Sc NUCLEUS

A ^{42}Sc nucleus is formed by an addition of one proton and one neutron to ^{40}Ca. This is the only odd-odd nucleus considered in the present paper. The configurations forming the yrast line of ^{42}Sc are shown in Fig. 10. The [1,1] configuration is built in valence space; it terminates at $I = 7^+$. The [2,2] configuration is an analog of the [1,1] configuration in ^{40}Ca but with an extra proton and extra neutron placed into the orbitals emerging from the $f_{7/2}$ spherical subshell. As a consequence, it has substantially larger deformation and maximum spin within the configuration than the [1,1] configuration in ^{40}Ca. At spin $I = 4\hbar$, the deformation of the [2,2] configuration is $\beta_2 \approx 0.27$ and $\gamma \approx -15^\circ$. It terminates at $I = 15^+$ in a terminating state with the structure $\pi(f_{7/2})^2_{6.0}(d_{3/2})^{-1}_{1.5} \otimes \nu(f_{7/2})^2_{6.0}(d_{3/2})^{-1}_{1.5}$ and near-spherical shape with $\beta_2 \approx 0.05$.

Additional excitations of the proton and neutron across the $Z = 20$ and $N = 20$ spherical gaps lead to a more deformed [3,3] configuration which has $\beta_2 \approx 0.37$ and $\gamma \approx -31^\circ$ at $I = 10\hbar$. It is expected to terminate at $I_{\rm max} = 23\hbar$ with the terminating state built at high energy cost and located above the yrast line. However, we were able to trace this configuration in the calculations only up to $I \approx 22\hbar$ (one $\hbar$ short of termination).

The lowest four SD configurations [4,4] in ^{42}Sc are formed from the yrast SD configuration [4,4] in ^{40}Ca by the addition of the proton and neutron to the $1/2[200](r = \pm i)$ orbitals located above the $Z = 20$ and $N = 20$ SD shell gaps (see Fig. 2). Their deformation properties are summarized in Fig. 11. Similar to the SD bands in ^{40}Ca, they are located in the $\gamma \approx -12^\circ$ minimum of potential energy surfaces. Note that the lowest [4,4] SD configuration undergoes unpaired band crossing [owing to the crossing of the $1/2[400](r = -i)$ and $1/2[200](r = -i)$ orbitals seen in Fig. 2], which leads to the [41,41] HD configuration.

At spin above $I = 22\hbar$, the HD configuration [41,41] becomes the lowest in energy. In this configuration, all single-particle states below the $Z = 21$ and $N = 21$ HD shell gap (Fig. 3) are occupied. So, contrary to the yrast HD bands in ^{40}Ca, which are degenerate in energy, the yrast HD line in

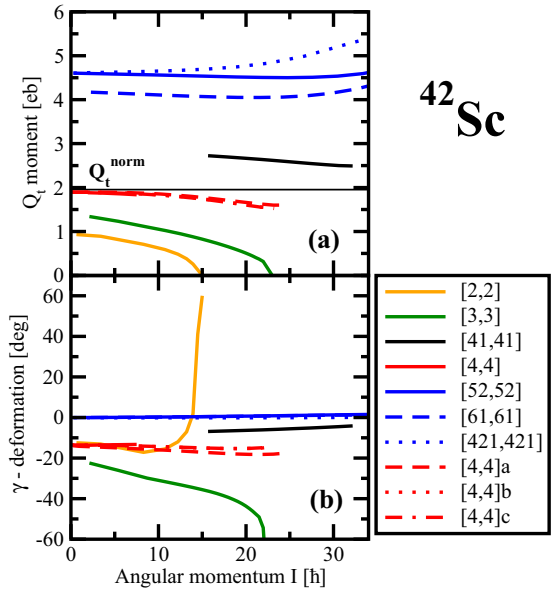

FIG. 11. The same as Fig. 5, but for ^{42}Sc.

^{42}Sc is represented by a single strongly decoupled branch of the [41,41] configuration.

At even higher spin (above $I = 30\hbar$), the yrast line is formed by the megadeformed configuration [421,421] (Fig. 10). This configuration contains the proton and neutron in the lowest megaintruder $N = 5$ orbital above the unpaired band crossing at $\Omega_x \approx 1.80$ MeV (above $I = 31\hbar$). At lower spin the structure of this MD configuration is [52,52]; this is a result of unpaired band crossing emerging from the interaction of the lowest megaintruder $(N = 5)(r = +i)$ orbital with the $1/2[321](r = +i)$ orbital taking place at $\Omega \approx 1.8$ MeV (Fig. 4). Note that this band crossing is blocked in the closely lying [52,52] MD configuration, shown by a solid blue line in Fig. 10, in which the 21st proton and 21st neutron are placed into the $1/2[321](r = -i)$ orbital located above the $Z = 20$ and $N = 20$ MD shell gaps.

Proton density distributions for the HD configuration [41,41] and MD configurations [52,52] and [421,421] are shown in Fig. 12. The major semiaxis ratio of the proton density distribution increases only moderately [from 2.23 to 2.65 (see Table I)] on going from the [41,41] configuration to the [52,52] one. However, this transition triggers drastic change in transition quadrupole moment Q_t; it is increased from $Q_t \approx 2.65\ e$b for the [41,41] configuration to $Q_t \approx 4.5\ e$b for the [52,52] configuration (see Fig. 11). The occupation of the megaintruder proton and neutron $N = 5$ orbitals leading to the MD [421,421] configuration creates both additional elongation of the proton density and neck in this density distribution (see bottom panels of Fig. 12). The [421,421] configuration is the most elongated structure studied in the present paper. Three-dimensional representation of its density distribution is shown in Fig. 1(a) of the Supplemental Material [78]. This density distribution has large semiaxis ratio of 3.40 at $I = 31$ which is increasing with spin (Table I). In part, this large value is a consequence of the development of the neck that leads to a small semiaxis in the direction perpendicular to elongation. Note that, despite a large difference in the semiaxis ratio (3.40 for the [421,421] configuration and 2.65 for the [52,52] one), the Q_t value of the [421,421] configuration ($Q_t \approx 5.2\ e$b at $I = 31\hbar$) is only by 15% larger that the one for the [52,52] configuration (see Fig. 11). These examples clearly indicate that there is no simple relation between the semiaxis ratio of the proton density distribution and transition quadrupole moments.

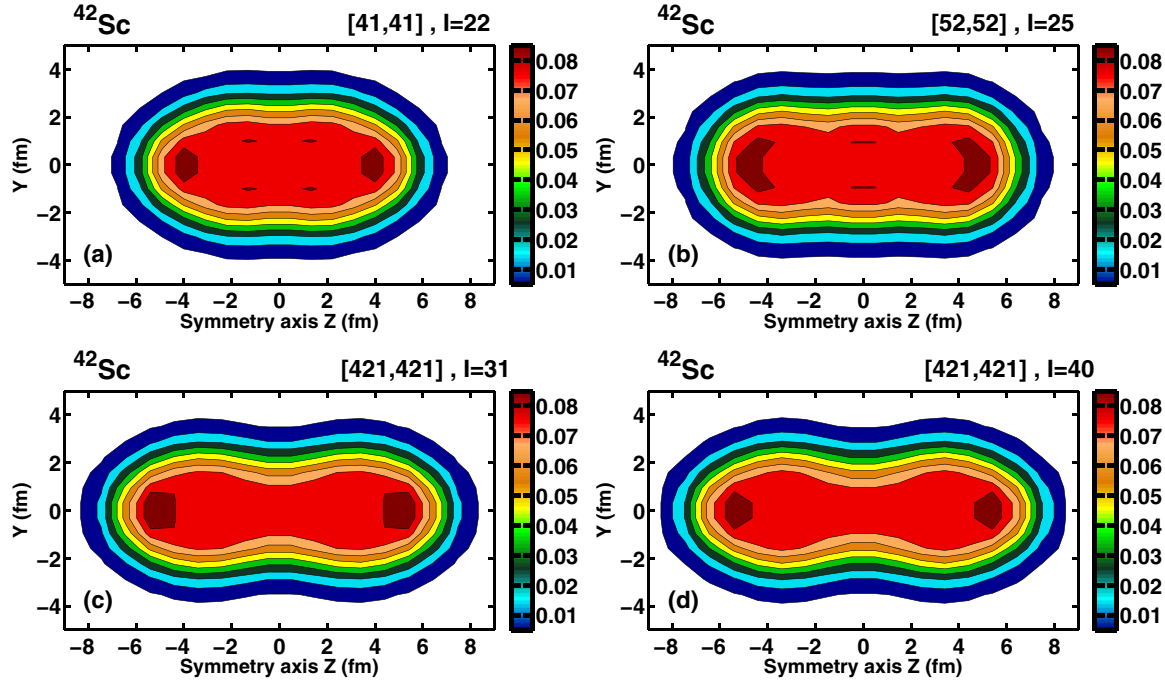

FIG. 12. The same as Fig. 8, but for ^{42}Sc.

TABLE I. The semiaxis ratios of the density distributions of the indicated configurations. They are defined only for plotted density distributions (see, for example, Fig. 8). The semiaxis ratios are extracted at $\rho_p = 0.04$ fm^{-3}, which corresponds roughly to half of the proton density in the central part of the nucleus. The type of configuration (SD, superdeformed; HD, hyperdeformed; MD, megadeformed) is shown in column 3.

Nucleus 1	Configuration, spin 2	Type 3	Semiaxis ratio 4
^{40}Ca	[4,4], $I = 12$	SD	2.05
	[41,41], $I = 24$	HD	2.27
	[42,42], $I = 25$	MD	2.90
^{42}Sc	[41,41], $I = 22$	HD	2.23
	[52,52], $I = 25$	MD	2.65
	[421,421], $I = 31$	MD	3.40
	[421,421], $I = 40$	MD	3.64
^{42}Ca	[4,4]a, $I = 21$	SD	2.17
	[62,42], $I = 0$	MD	2.72
	[62,42], $I = 16$	MD	2.79
^{44}Ca	[62,42], $I = 27$	MD	2.39
^{44}Ti	[41,41], $I = 25$	SD	2.03
	[62,62], $I = 0$	MD	2.70
	[62,62], $I = 32$	MD	2.88
^{46}Ti	[62,51], $I = 26$	SD	1.75
	[62,42], $I = 28$	HD	2.40
^{48}Cr	[62,62], $I = 0$	HD	2.24
	[62,62], $I = 28$	HD	2.39
^{50}Cr	[62,62], $I = 31$	HD	2.27
^{36}Ar	[2,2], $I = 4$	SD	1.9
	[4,4], $I = 16$	HD	2.21
	[31,31], $I = 21$	MD	2.56
	[41,41], $I = 30$	MD	2.64
^{38}Ar	[3,2]a, $I = 12$	SD	1.91
	[42,31], $I = 24$	HD	2.27
	[42,31], $I = 32$	MD	2.74
^{32}S	[2,2], $I = 12$	SD	2.09
	[21,21], $I = 31$	HD	2.15
^{34}S	[2,1], $I = 14$	SD	1.32
	[31,21], $I = 21$	HD	2.32

V. THE GENERAL FEATURES OF HIGH-SPIN SPECTRA

The discussion of low-spin spectra in Secs. III and IV clearly shows the importance of particle-hole excitations across the $N = 20$ and $Z = 20$ spherical shell gaps in building angular momentum and deformation. The most striking example is ^{40}Ca, in which only the ground state could be built in the valence space. Here the valence space is defined as the configuration space which does not involve particle-hole excitations across either the $N = 20$ and $Z = 20$ spherical shell gaps or the $N = 28$ and $Z = 28$ spherical shell gaps.

The maximum spin that could be built in the valence space of nuclei is summarized in Table II. It is defined with respect to a spherical ^{40}Ca core by the occupation of proton and neutron $f_{7/2}$ orbitals in the Ca, Sc, Ti, and Cr nuclei and by the proton and neutron holes in the $N = 2$ $d_{3/2}$, $s_{1/2}$, and $d_{5/2}$ orbitals in the Ar and S nuclei. One can see that the maximum spin increases on approaching the middle of the $f_{7/2}$ subshell, where it reaches the maximum value of $I_{\max} = 16\hbar$ in the $\pi(f_{7/2})^4_{8.0} \otimes \nu(f_{7/2})^4_{8.0}$ configuration of ^{48}Cr. Note that the addition of two neutrons to this configuration decreases the maximum spin which could be built in the valence space of ^{50}Cr (see Table II).

TABLE II. The maximum spin (in $\hbar$) that could be built within the configuration of given type. The asterisk is used to indicate the configurations which involve the hole(s) in the $d_{5/2}$ orbital(s). The SD configurations are not included into this table. See text for the discussion of the details.

Nucleus 1	Valence space 2	2p-2h 3	4p-4h 4
^{40}Ca	[0,0], $I_{\max} = 0$	[1,1], $I_{\max} = 10$	[2,2], $I_{\max} = 20$*
^{42}Ca	[2,0], $I_{\max} = 6$	[3,1], $I_{\max} = 14$	[4,2], $I_{\max} = 24$*
^{44}Ca	[4,0], $I_{\max} = 8$	[5,1], $I_{\max} = 14$	[6,2], $I_{\max} = 20$*
^{42}Sc	[1,1], $I_{\max} = 7$	[2,2], $I_{\max} = 15$	[3,3], $I_{\max} = 23$*
^{44}Ti	[2,2], $I_{\max} = 12$	[3,3], $I_{\max} = 18$	[4,4], $I_{\max} = 24$*
^{46}Ti	[4,2], $I_{\max} = 14$	[5,3], $I_{\max} = 19$	[6,4], $I_{\max} = 22$*
^{48}Cr	[4,4], $I_{\max} = 16$	[5,5], $I_{\max} = 20$*	[6,6], $I_{\max} = 20$*
^{50}Cr	[6,4], $I_{\max} = 14$	[7,5], $I_{\max} = 16$*	
^{36}Ar	[0,0], $I_{\max} = 8$*	[1,1], $I_{\max} = 16$*	
^{38}Ar	[0,0], $I_{\max} = 4$*	[1,1], $I_{\max} = 14$*	
^{32}S	[0,0], $I_{\max} = 12$*	[1,1], $I_{\max} = 20$*	
^{34}S	[0,0], $I_{\max} = 10$*	[1,1], $I_{\max} = 19$*	

Table II also illustrates how the maximum spin, which could be built within the configuration, changes when particle-hole excitations across the spherical $Z = 20$ and $N = 20$ spherical shell gaps are involved. Here 2p-2h configurations are defined as the configurations which involve the excitations of one proton and one neutron across the respective shell gaps. The excitations of two protons and two neutrons across these gaps lead to the 4p-4h configurations. The impact of these excitations on the maximum spin depends on how many occupied $f_{7/2}$ orbitals in the Ca, Sc, Ti, and Cr nuclei (or holes in the $N = 2$ orbitals of the Ar and S nuclei) the nucleus has in its valence space. One can see that these excitations increase drastically the maximum spin within the configurations of ^{40}Ca but have limited impact on maximum spin in ^{48}Cr (Table II).

The analysis of the ^{40}Ca and ^{42}Sc nuclei clearly indicates that subsequent particle-hole excitations lead to the yrast or near-yrast SD, HD, and MD configurations at the spins which are either similar to the maximum spins that could be built within the 2p-2h and 4p-4h configurations or slightly above them. Note that the nuclei in these 2p-2h and 4p-4h configurations could at most be described as highly deformed.

The importance of these 2p-2h and 4p-4h configurations lies in the fact that at low and medium spins they dominate the yrast line and thus are expected to be populated in experiment with high intensity. The observation of the SD, HD, and MD configurations requires that these bands are either yrast or close to yrast at the spins where the feeding of the bands takes place. This is especially critical for the HD and MD bands because in most of the nuclei they have completely different slope in the E-$E_{\rm RLD}$ plots than in the bands of smaller deformation. As a result, their excitation energies with respect to the yrast

line grow up very rapidly with decreasing spin below the spins where the HD and MD bands are yrast or near yrast. This factor will limit the spin range in which they can be observed in future experiments to the spin range in which these bands are either yrast or close to yrast and few states below this spin range.

Considering the limitations of experimental facilities to observe high-spin states in light nuclei, it is imperative that expected candidates for the SD, HD, and MD bands become yrast (or close to yrast) at the spins which are not far away from currently measured. Indeed, with the current generation of detectors the SD bands in ^{36}Ar [25] and ^{40}Ca [22] and ground state band in ^{48}Cr [77] are observed up to $I = 16\hbar$, which represents the highest spin measured in this mass region. The advent of γ-tracking detectors such as GRETA and AGATA will increase the spin up to which the measurements could be performed, but this increment in spin is not expected to be drastic.

Note that the results discussed in this section only illustrate the general features of rotating nuclei and provide some crude estimates of the competition of terminating and extremely deformed configurations. Indeed, detailed calculations are needed to define the properties of such bands and the spins at which extremely deformed configurations become yrast. For the sake of simplicity, we also do not discuss here possible excitations across the spherical $N = 28$ and $Z = 28$ shell gaps. Terminating configurations based on such excitations compete with the SD, HD, and MD configurations only in ^{46}Ti and Cr nuclei (see Secs. VI D, VI E, and VI F below).

The examples of the ^{40}Ca and ^{42}Sc nuclei discussed above once more confirm that rotating nuclei are the best laboratories for studying the shape coexistence. Indeed, starting from either spherical or weakly deformed ground states by means of subsequent particle-hole excitations, one can build any shape (prolate, oblate, triaxial, and super-, hyper-, and megadeformed, as well as cluster and/or molecular structures [see Sec. VII for a discussion of latter structures and/or shapes]) in the same nucleus.

VI. OTHER NUCLEI IN THE NEIGBORHOOD OF ^{40}Ca

The results for other nuclei studied in this paper are presented in this section. In the calculations of terminating structures at low and medium spins we concentrate on the configurations which define the general structure of the yrast line and the spins at which the transition to extremely deformed configurations takes place. Apart from a few interesting cases, we do not discuss them in detail. The main focus of this section is the super-, hyper-, and megadeformed rotational configurations and, in particular, the ones which potentially show the features of clusterization and molecular structures. To provide the guidance for future experiments, we present the (E-$E_{\rm RLD}$) plots and the figures with transition quadrupole moments and γ deformations for each nucleus. In addition, the proton density plots are provided for the yrast or near-yrast configurations which could be measured in future experiments. The goals behind that are to see the evolution of the density distribution with configuration and nucleus and to find interesting candidates for clusterization and molecular structures. Note that some graphical results of the calculations are provided in the Supplemental Material with this article as Ref. [78].

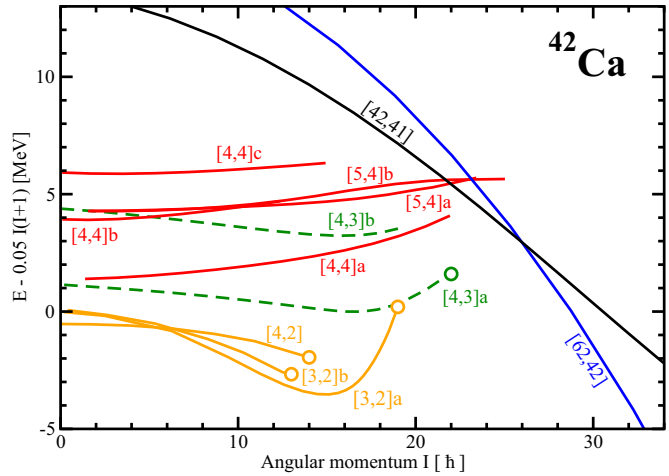

FIG. 13. The same as Fig. 1, but for ^{42}Ca.

A. ^{42}Ca nucleus

The energies of calculated configurations are shown in Fig. 13. The calculated transition quadrupole moments and γ deformations of these configurations are displayed in Fig. 14. Note that this nucleus has two extra neutrons as compared with ^{40}Ca, which affects the structure of the configurations.

The SD configurations are represented by the [4,4]a, [4,4]b, [4,4]c, [5,4]a, and [5,4]b configurations (Fig. 13). The yrast [4,4]a SD configuration in ^{42}Ca is formed by an addition of two extra neutrons in the 1/2[200] orbitals [located above the $N = 20$ SD shell gap (Fig. 2)] to the yrast [4,4] SD configuration of ^{40}Ca. Note that similar to ^{40}Ca the SD configurations in ^{42}Ca are triaxial with $\gamma \approx -12^\circ$.

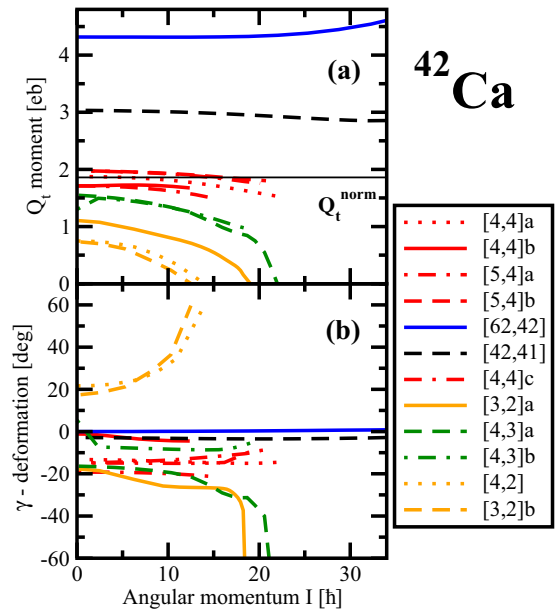

FIG. 14. The same as Fig. 5, but for ^{42}Ca.

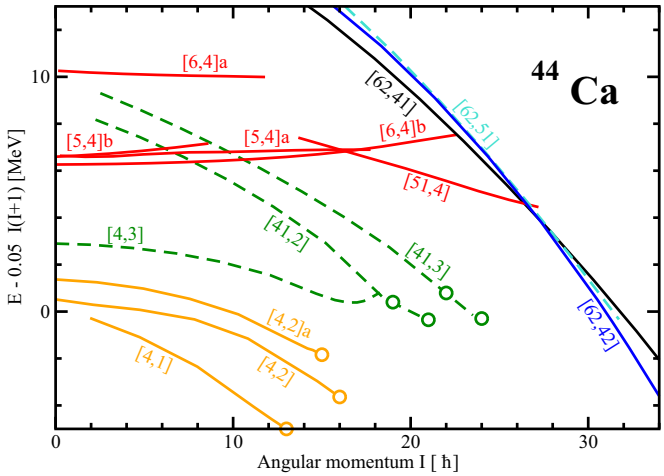

FIG. 15. The same as Fig. 1, but for ^{44}Ca. Note that for some configurations several aligned (terminating) states can be formed; the reasons for their formation are discussed in Sec. 6.6 of Ref. [20].

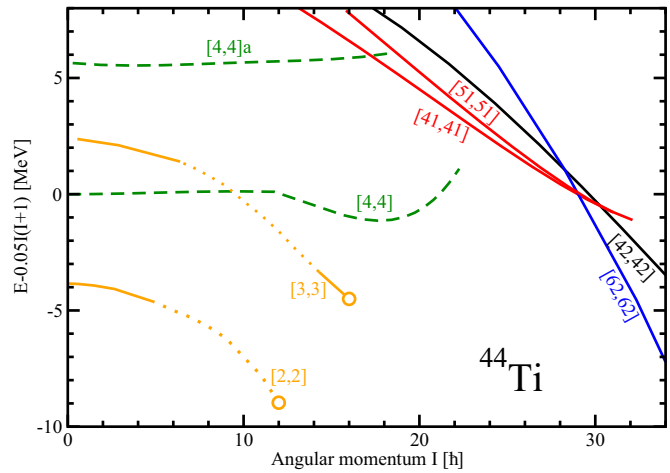

FIG. 16. The same as Fig. 1, but for ^{44}Ti. Note that it was not possible to trace the middle parts of the [2,2] and [3,3] configurations in the calculations. Thus, they are shown by dotted lines.

At spin $I \approx 23\hbar$, the expected continuation of the SD [4,4] configuration is crossed by the HD [42,41] configuration, which is formed from the yrast HD [41,41] configuration in ^{40}Ca (Fig. 3) by adding one neutron into the $1/2[440](r = +i)$ orbital and another into the $5/2[202](r = +i)$ orbital. The HD [42,41] configuration has near prolate shape with the Q_t value, which exceed by 50% the Q_t values which are typical for the SD bands (Fig. 14).

Axially symmetric MD configuration [62,42] becomes yrast above $I = 26\hbar$ (Fig. 13). At these spins, its transition quadrupole moment is by ≈50% larger than that of the HD [42,41] configuration (Fig. 14).

Proton density distributions of the yrast SD [4,4]a and MD [62,42] configurations are shown in Fig. 2(a) of the Supplemental Material [78] and Figs. 33(c) and 33(d) below, respectively. The major semiaxis ratio is 2.17 and 2.79 for these configurations (Table I). However, the Q_t values of the latter configuration are by a factor of more than 2 larger than those of the former one (Fig. 14).

B. ^{44}Ca nucleus

The SD configurations are represented by the [6,4] and [51,4] configurations (Fig. 15). However, up to spin $I \approx 22\hbar$ the total yrast line is formed by the normal and highly deformed triaxial terminating configurations and these SD configurations are located at high excitation energy with respect to the total yrast line. Only around $I \approx 24\hbar$ does the [51,4] SD configuration become yrast. However, already at spin $I = 26\hbar$ and above the yrast line is formed by closely lying [62,41] HD and [62,42] MD configurations.

The calculated values of the transition quadrupole moment Q_t of these configurations are shown in Fig. 3 of the Supplemental Material [78]. Proton density distribution of the MD [62,42] configuration is displayed in Fig. 2(b) in the Supplemental Material [78]. The [62,51] configuration, shown by a dashed cyan line in Fig. 15, is lying closely in energy to these two configurations. Its calculated Q_t values are between the ones for the HD and MD configurations (see Fig. 3 in the Supplemental Material [78]).

The yrast line of ^{44}Ca shows that with increasing neutron number up to $N = 24$ (which leads to the placement of the neutron Fermi level in the middle of deformed single-particle states emerging from spherical $1f_{7/2}$ subshell) it becomes energetically favorable to excite the neutron across the spherical $N = 28$ shell gap. Such excitation leads to the occupation of the lowest $1g_{9/2}$ neutron orbital (which carries substantial single-particle angular momentum) and, in the case of ^{44}Ca, to the formation of the [41,2] and [41,3] configurations which terminate at spins $I = 21$, 22, and $24\hbar$ (Fig. 15). As a consequence, the yrast line could be built by either normal or highly deformed terminating configurations up to higher spins in ^{44}Ca as compared with lighter Ca isotopes (compare Figs. 15, 13, and 1). As a result, the observation of the SD, HD, and MD configurations would be more difficult in heavier Ca isotopes as compared with ^{40}Ca. Note that this mechanism of neutron excitations across the $N = 28$ spherical shell gap affects also the yrast line in ^{46}Ti (configuration [41,4], Fig. 18). Similar proton excitation across the $Z = 28$ spherical shell gap become active in the Cr isotopes. Indeed, the configurations of the type [*1,*1] built on simultaneous neutron and proton excitations across the $N = 28$ and $Z = 28$ spherical shell gaps are active in the creation of the yrast line at medium spin in ^{48,50}Cr (see Figs. 20 and 21 below).

C. ^{44}Ti nucleus

The SD configurations are represented by the [41,41] and [51,51] configurations (see Figs. 16 and 17). These configurations are either yrast or very close to the yrast line above $I = 24\hbar$ after the crossing with the expected continuation of the [4,4] configuration. The [4,4] and [4,4]a configurations may also be considered as SD at low spin because they are located at the borderline between the SD and highly deformed bands. The increase of the proton and neutron numbers to 22 leads to a decrease of the impact of

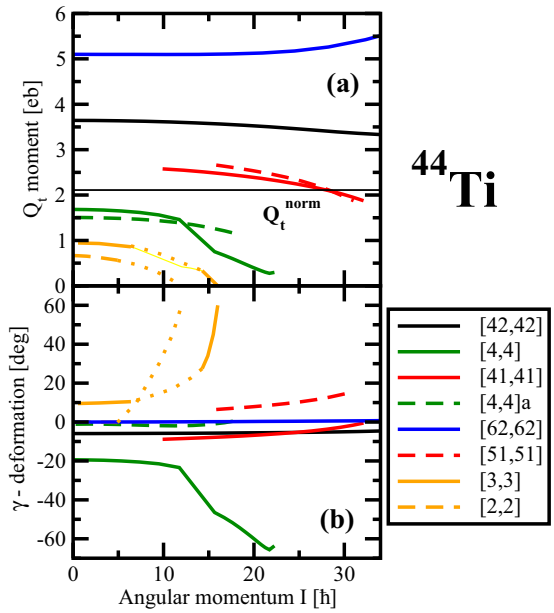

FIG. 17. The same as Fig. 5, but for ^{44}Ti.

the hyperintruder $N = 4$ orbitals. Indeed, the [41,41] and [51,51] configurations have transition quadrupole moments Q_t which are only slightly above the one typical for the SD configurations (Fig. 17).

Only the occupation of additional proton and neutron $N = 4$ hyperintruder orbitals leads to the configuration [42,42] (see Fig. 16) that is truly hyperdeformed (Fig. 17). However, the HD configurations are never yrast in this nucleus. At spin $I \approx 29\hbar$, the MD [62,62] configuration becomes yrast. The proton density distribution of this configuration [see Figs. 33(e) and 33(f) below] could be compared with the one for the SD [41,41] configuration (see Fig. 2(c) in the Supplemental Material [78]). Its three-dimensional representation is shown in Fig. 1(b) of the Supplemental Material [78]. The Q_t value of the MD configuration is larger than the one for the SD configuration by a factor of approximately 2.5 (Fig. 17). However, the difference in the ratio of major semiaxes of the density distributions of these two configurations is smaller [the major semiaxis ratio is 2.88 for the [62,62] configuration and 2.03 for the [42,42] configuration (Table I)].

D. ^{46}Ti nucleus

As discussed in Sec. VI B, the increase of neutron number to $N = 24$ leads to a situation in which the particle-hole excitations across the $N = 28$ spherical shell gap create the configurations which contribute to the yrast line at medium spin (the [4,4] configuration terminating at $I = 25\hbar$, Fig. 18). At higher spin the SD [62,51]a configuration becomes yrast. The HD [62,42] configuration is only slightly excited in energy with respect to this configuration. Proton density distributions of these two configurations are shown in Figs. 2(d) and 2(e) of Supplemental Material [78]. Note that the MD configurations are not energetically favored in this nucleus and they do not show up in the vicinity of the yrast line in the spin range of

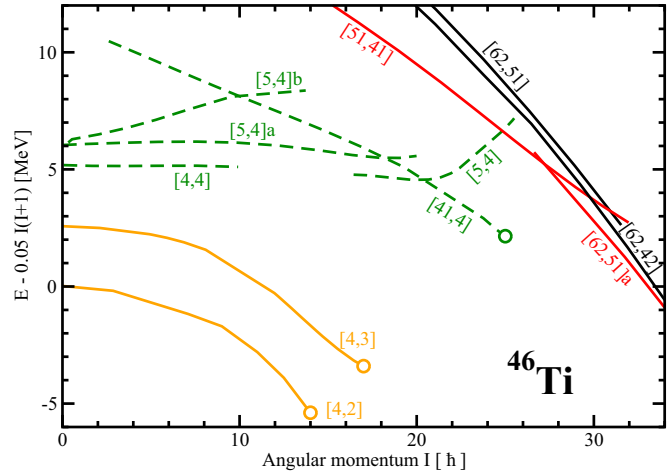

FIG. 18. The same as Fig. 1, but for ^{46}Ti.

interest. The calculated Q_t and γ-deformation values of the configurations displayed in Fig. 18 are summarized in Fig. 19.

E. ^{48}Cr nucleus

The valence space terminating [4,4] configuration is forming the yrast line up to $I = 16\hbar$ (Fig. 20). This band has been observed in experiment up to its termination in Ref. [77]. Particle-hole excitations across the $Z = 20$ and $N = 20$ spherical shell gaps lead to only marginal increase of angular momentum content of the configurations but cost a lot of energy (see, for example, the configurations [4,5] and [5,5] in Fig. 20 and Table II). Higher spin configurations are built at a reasonable energy cost by particle-hole excitations across the $Z = 28$ and $N = 28$ spherical shell gaps. Such excitations lead both to terminating and SD/HD configurations. The first type of configurations is represented by the [41,41]

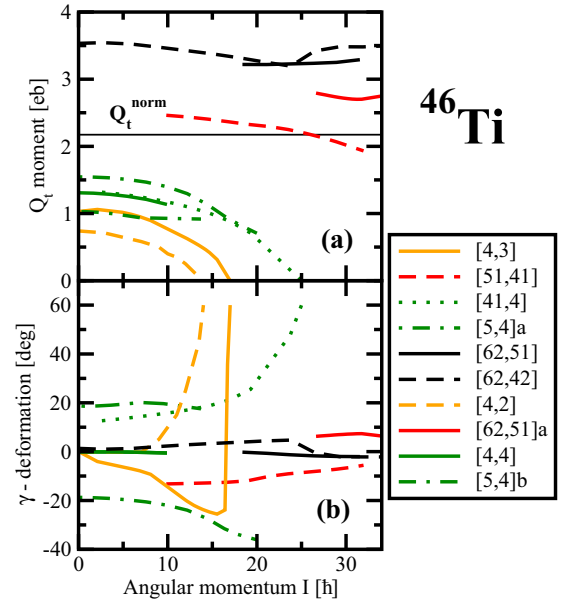

FIG. 19. The same as Fig. 5, but for ^{46}Ti.

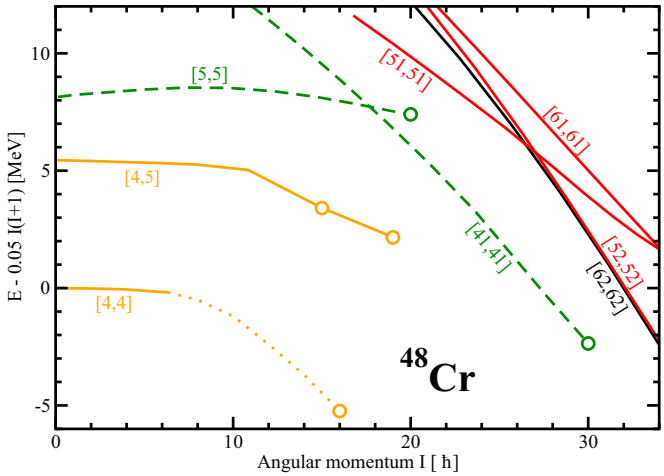

FIG. 20. The same as Fig. 1, but for ^{48}Cr.

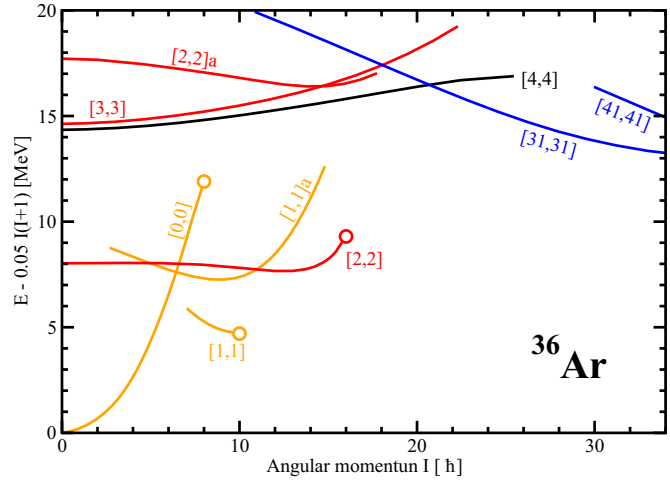

FIG. 22. The same as Fig. 1, but for ^{36}Ar.

one which terminates at $I = 30\hbar$. The SD [52,52] and HD [62,62] configurations lying at similar energies become the lowest configurations at spin $I \geqslant 30\hbar$ (Fig. 20). Note that the resonance observed at $I \approx 36\hbar$ in the ^{24}Mg + ^{24}Mg reaction strongly supports a HD shape for a compound ^{48}Cr nucleus formed in this reaction [30]. The evolution of proton density distribution with spin in the [62,62] configuration is shown in Figs. 2(f) and 2(g) of the Supplemental Material [78]. The Q_t and γ-deformation values are summarized in Fig. 5 of the Supplemental Material.

F. ^{50}Cr nucleus

The calculated configurations are shown in Fig. 21. Below spin $I = 14\hbar$, the yrast line is built from valence space [6,4] configuration. Higher spin terminating configurations ([51,4], [51,31], and [51,41]) are built by means of particle-hole excitations across the $Z = 28$ and $N = 28$ spherical shell gaps. They dominate the yrast line up to $I = 31\hbar$. At even higher spin closely lying HD [62,62] and [72,62] configurations are either yrast or close to yrast. Transition

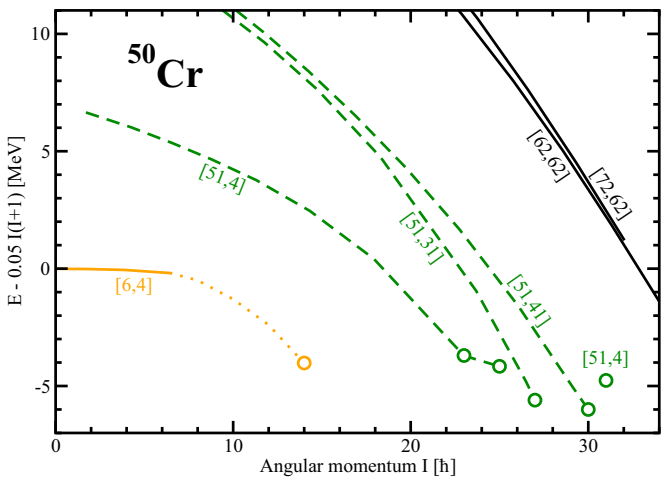

FIG. 21. The same as Fig. 1, but for ^{50}Cr.

quadrupole moments Q_t and γ deformations of the calculated configurations are summarized in Fig. 6 of the Supplemental Material [78]. An example of proton density distribution is shown in Fig. 2(h) of the Supplemental Material for the HD [62,62] configuration at $I = 31\hbar$ [78]. Note that neither superdeformed nor megadeformed configurations show up in the vicinity of the yrast line in this nucleus in the spin range of interest.

G. ^{36}Ar nucleus

The maximum spin which could be built in the valence space of this nucleus is quite limited, namely, $8\hbar$ in the [0,0] configuration (Fig. 22 and Table II). Particle-hole excitations leading to the [1,1] configurations increase this spin up to $16\hbar$ (configuration [1,1]a in Fig. 22). Subsequent particle-hole excitations generate the [2,2] configurations, the maximum spin within which is $20\hbar$ (see Table II).

One such configuration terminating at $I = 16\hbar$ is assigned to the SD band observed in Refs. [25,26]. Its properties have been studied earlier within the spherical shell model [79] and cranked Nilsson-Strutinsky approach [25,26]. Based on the calculated deformation properties, this configuration could be considered as SD only at low spin. This is because with increasing spin its transition quadrupole moment Q_t is decreasing rapidly and γ deformation is increasing up to $\gamma = 60^\circ$ (Fig. 23). The terminating state of this configuration/band is reached at $I = 16^+$ both in theory (Fig. 22) and in experiment (Refs. [25,26]). From our point of view, the classification of this band as highly deformed triaxial is more appropriate but we label it as SD in Fig. 1 following the classification established in the literature.

At spin above $I = 16\hbar$, the yrast line is built from the HD [4,4] and MD [31,31] configurations. It is easy to understand the structure of these configurations from the Routhian plot for the [42,42] MD configuration in ^{40}Ca (Fig. 4). The [4,4] configuration in ^{36}Ar is built by removing two protons and two neutrons in the $N = 4$ orbitals from the MD [42,42] configuration in ^{40}Ca. The [31,31] configurations in ^{36}Ar are built by removing one proton and one neutron in the $N = 4$

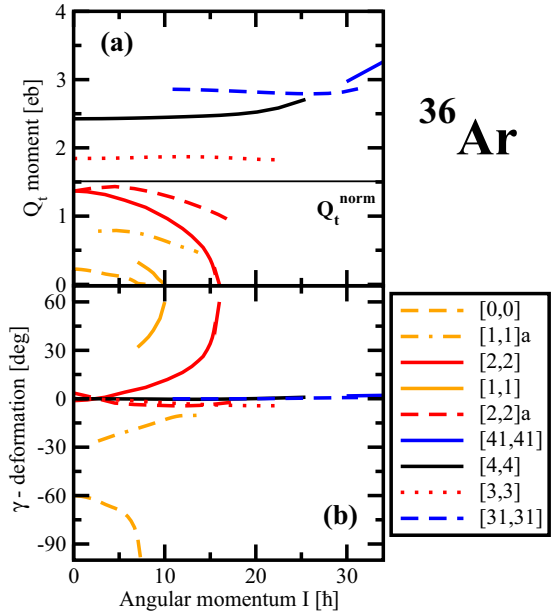

FIG. 23. The same as Fig. 5, but for ^{36}Ar.

orbital from the [42,42] configuration in ^{40}Ca and another proton and another neutron from the 3/2[321] orbital of the same configuration. Because opposite signature branches of the 3/2[321] orbital are either degenerate in energy (as in Fig. 4) or have very small energy splitting, four [31,31] configurations are calculated at close energies. For simplicity, we show only the lowest one in Fig. 22.

Note that in many calculations these extremely deformed structures do not form a stable minimum in the potential energy surfaces at spin zero (see, for example, Fig. 2 in Ref. [12]). Thus, the rotation helps to stabilize this minimum. This is similar to the situation with the stabilization of hyperdeformation at high spin in medium-mass nuclei (Ref. [19]).

The transition quadrupole moments Q_t and γ deformations of the calculated configurations are summarized in Fig. 23. One can see that the Q_t values of the [4,4] and [31,31] MD configurations are by approximately 66% and 100% larger than the normalized transition quadrupole moment $Q_t^{\rm norm}$ for the SD shapes. Proton density distributions of the SD [2,2] (at low spin), HD [4,4], and MD [31,31] and [41,41] configurations are shown in Fig. 24 (see also Table I for the density semiaxis ratios). Three-dimensional representation of the proton density distribution in the MD [31,31] configuration is shown in Fig. 1(c) of the Supplemental Material [78]. The SD shapes are characterized by more compact (with higher average density in the interior of the nucleus) density distribution than those of the HD and MD shapes (Fig. 24). The formation of the necking degree of freedom is clearly seen in the MD [31,31] and [41,41] configurations.

The results obtained in the cranked Nilsson-Strutinsky (CNS) approach are very similar to the CRMF ones (see Fig. 6 in Ref. [41]). Indeed, the MD [31,31] configurations are yrast above spin $I = 18\hbar$ also in the CNS calculations. Considering that both experimental data in this nucleus extend up to $I = 16^+$ and yrast or near-yrast higher spin configurations are formed from HD and/or MD ones, the calculations in the CRMF and CNS frameworks clearly indicate this nucleus as one of the best candidates for the observation of the hyper- and megadeformations. In simple words, if it will be possible to bring higher (than $16\hbar$) angular momentum into this system, the population of the HD and MD states is the most likely outcome of this process.

H. ^{38}Ar nucleus

The low-spin yrast line in this nucleus is built from terminating configurations (Fig. 25). The lowest SD configuration [3,2]a is close to the yrast line at medium spin and it becomes yrast above $I = 17\hbar$ (Fig. 25). Similar to the observed SD band in ^{36}Ar, it terminates in the noncollective state but at a higher spin of $I = 22\hbar$. Its proton density distribution at the medium spin of $I = 12\hbar$ is shown in Fig. 3(a) of the Supplemental Material [78]. The yrast line above $I = 22\hbar$ is built from the [42,31] MD signature partner configurations with small energy splitting (Fig. 25). They differ in the occupation by the third proton of different signatures of the 3/2[321] orbital; there is almost no signature splitting between the different signatures of this orbital (see Fig. 4). An interesting feature of this configuration is the substantial impact of rotation on the density distribution leading to a larger elongation and more pronounced necking with increasing spin from $I = 24\hbar$ to $I = 32\hbar$ [see Figs. 33(a) and 33(b) below]. This, however, is not associated with the substantial change of transition quadrupole moment Q_t (Fig. 26).

I. ^{32}S nucleus

The SD configurations were predicted in ^{32}S a long time ago in Refs. [80,81]. The SD bands built on such structures have been studied both in nonrelativistic cranked DFTs based on the Gogny [40,82] and Skyrme [37,39] forces and in the CRMF calculations with the NL3 CEDF in Ref. [41]. The detailed structure of the yrast spectra of this nucleus has also been investigated in the CNS approach in Ref. [41]. Note that, contrary to more microscopic studies, which are limited to collective structures, this CNS study considers also terminating/aligned states along the yrast line, which is important for a proper description of the yrast line at low and medium spins.

Figure 27 shows the high-spin structures in ^{32}S. The lowest SD configuration with the structure [2,2] is yrast above spin $I = 10\hbar$. The same result has also been obtained in other models quoted above. Above spin $I = 24\hbar$, the occupation of the lowest $N = 4$ hyperintruder proton and neutron orbitals leads to the HD [21,21] configuration. Note that this induces an unpaired band crossing, the consequence of which is the impossibility to trace in the calculations the SD band above $I \approx 23\hbar$ and HD band below $I \approx 27\hbar$. This problem could be avoided if diabatic orbitals would be built using an approach of Ref. [20]; the expected diabatic continuations of the SD [2,2] and HD configurations [21,21] are shown by dotted lines in Fig. 27. Note that the CNS calculations of Ref. [41] also suggest that the lowest HD configuration has the [21,21] structure and becomes yrast at similar spins. The same HD

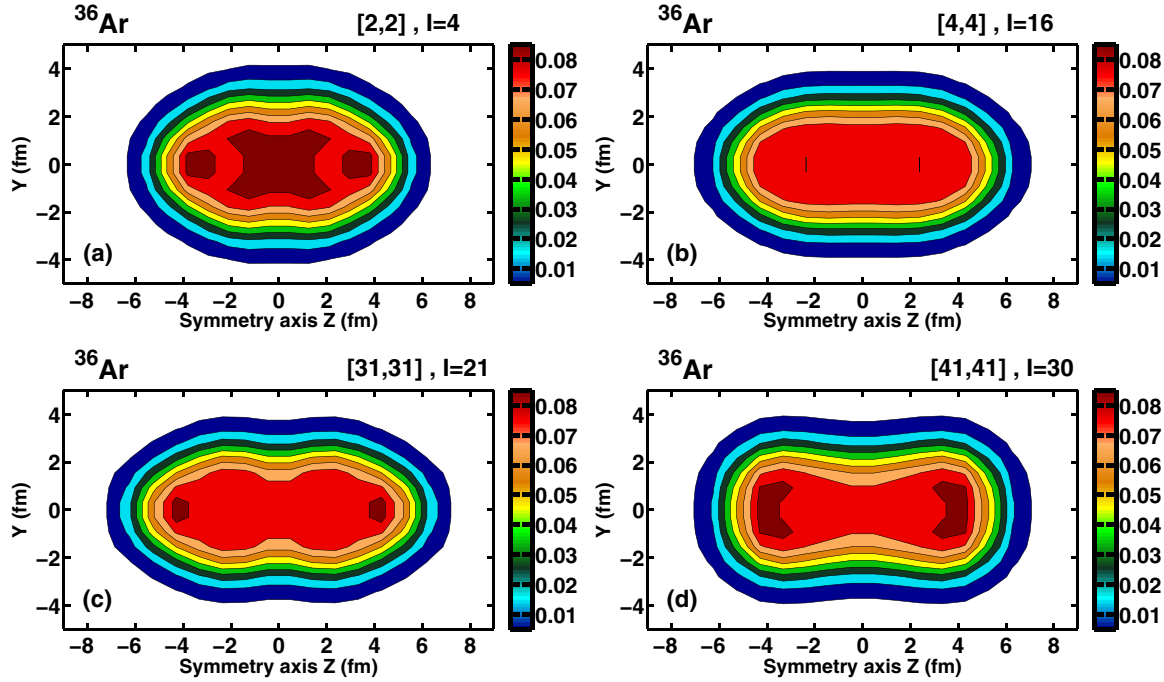

FIG. 24. The same as Fig. 8, but for ^{36}Ar.

configuration has also been obtained in cranked Skyrme HF calculations of Ref. [37]; it also becomes yrast around $I \approx 25\hbar$ in the calculations with SIII and SkM* Skyrme forces.

At spin $I = 0$, the calculated Q_t values for the [2,2] SD configuration are 50% larger than $Q_t^{\rm norm}$ (Fig. 28). This would even make it possible to describe this band as HD. However, at this spin the [2,2] SD configuration is located around 10 MeV above the ground state, which prevents its observation. The rotation and the limited angular momentum content in low-deformation configurations brings this SD configuration to the yrast line. However, it also triggers the decrease of the collectivity (as measured by Q_t), so this configuration is more properly described as SD in the spin range where it is yrast. The occupation of the lowest $N = 4$ proton and neutron orbitals leading to the [21,21] HD configuration triggers substantial increase of Q_t; at spin $I = 31\hbar$ it is by 60% larger than the $Q_t^{\rm norm}$. Density distributions of the [2,2] and [21,21] configurations at spins of interest are shown in Fig. 29. Note that many [1,1] configurations are of transitional type; they are SD only at very low spins (Fig. 28) and are only highly deformed at higher spins. Truly SD configurations are obtained with additional occupation of the $N = 3$ orbital leading to either [2,1] or [1,2] configurations (Fig. 28).

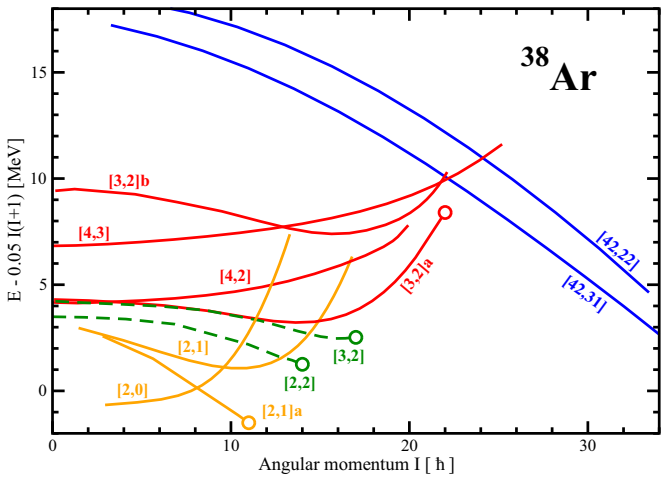

FIG. 25. The same as Fig. 1, but for ^{38}Ar.

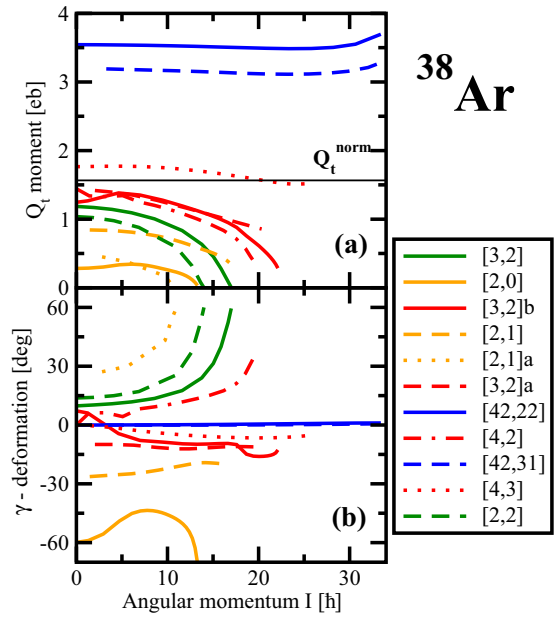

FIG. 26. The same as Fig. 5, but for ^{38}Ar.

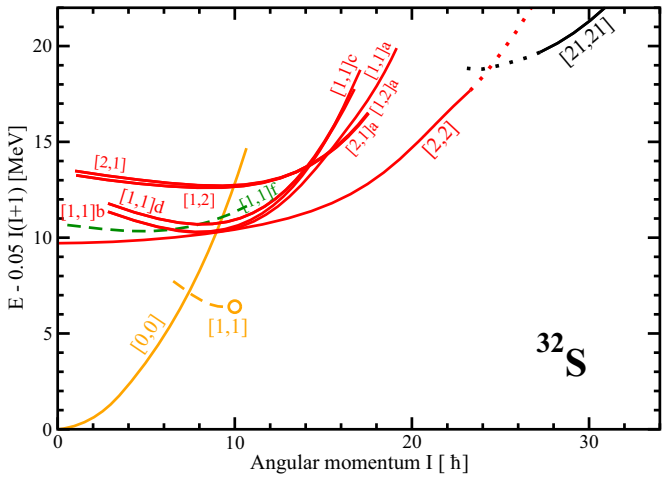

FIG. 27. The same as Fig. 1, but for ^{32}S. Dotted lines show expected diabatic continuations of the [2,2] and [21,21] configurations beyond the spin range where the convergence has been obtained.

Present calculations indicate a large gap between the yrast SD [2,2] configuration and excited configurations in the spin range $I = 16\hbar$–$22\hbar$ (Fig. 27). Although this would favor the population of this configuration, all experimental attempts to observe this band undertaken in the beginning of the last decade have failed.

J. ^{34}S nucleus

The configurations in the ^{34}S nucleus are formed from the ones in ^{32}S by adding two neutrons in respective orbitals. The [2,1] configurations in ^{34}S are similar to the [1,1] ones in ^{32}S; they are SD at low spin but lose the collectivity with increasing spin so that they are better described as highly deformed at the highest calculated spins (see Fig. 31 below).

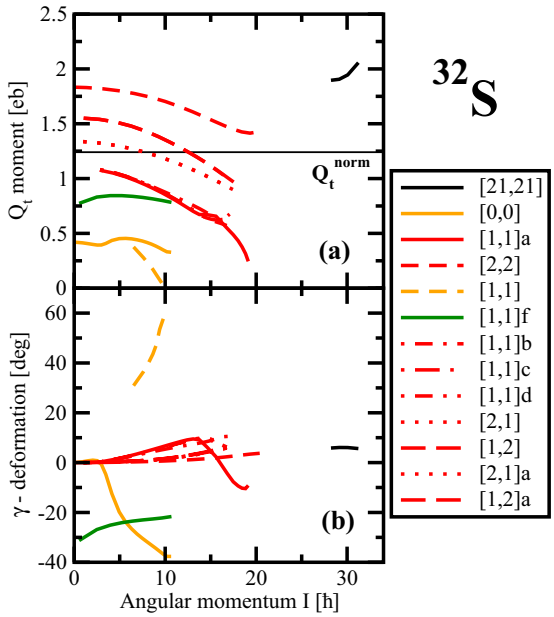

FIG. 28. The same as Fig. 5, but for ^{32}S.

Indeed, their density distributions at medium and high spins are characterized by a rather modest semiaxis ratio; this is seen in Fig. 3(b) of the Supplemental Material [78] on the example of the [2,1] configuration which has a semiaxis ratio of 1.32 (see Table I) at $I = 14\hbar$. Similar to ^{32}S, truly SD shapes are formed with the occupation of at least two $N = 3$ protons and two $N = 3$ neutrons. They are represented by the [2,2] SD configuration [which is yrast above $I = 16\hbar$ (see Fig. 30)] and by the excited [3,2] and [3,2]a SD configurations. The occupation of the lowest $N = 4$ neutron and proton orbitals leads to the HD configurations [31,21] and [31,11]. The first configuration is yrast at spin $I = 20\hbar$ and above (Fig. 30) and its proton density distribution is shown in Fig. 32.

VII. CLUSTERIZATION AND MOLECULAR STRUCTURES

One of the main goals of the present paper is the search for possible candidates showing clusterization and molecular structures in the near-yrast region of the nuclei under study. Different single-particle states have different spatial density distributions which are dictated by their underlying nodal structure of their wave functions (see Fig. 9 in Ref. [47]); the centers of the density distribution are found at the nodes and peaks of the oscillator eigenfunctions. The total density distribution is built as a sum of the single-particle density distributions of occupied single-particle states. Thus, for some specific occupations of the single-particle states at some deformations, one may expect the effects in the density distributions which could be interpreted in terms of clusterization and molecular structures. Note that the structure of the wave functions of the single-particle orbitals is affected by rotation (see discussion in Sec. V of Ref. [47]); this could lead to a modification of the single-particle density distributions (see Fig. 9 in Ref. [47]). For some of the orbitals the effect of rotation on single-particle density distributions is quite substantial, while it has very little impact on the single-particle density distributions for others. This could lead either to a destruction or the emergence/enhancement of the clusterization and molecular structures with rotation.

A well-known case of molecular structure in this mass region is the superdeformed configuration [2,2] in ^{32}S; according to Refs. [3,11] the wave function of this band contains a significant admixture of the molecular ^{16}O + ^{16}O structure. Indeed, the development of a neck is seen in its density distribution [Fig. 29(a)]. A similar neck exists also in the HD [21,21] configuration of ^{32}S [Fig. 29(b)], but the presence of density depressions at $z \approx \pm 2$ fm may suggest a more complicated structure than the pair of two ^{16}O. In addition, the neck is also present in the density distribution of the [31,21] configuration in ^{34}S, but this configuration is characterized by an unusual density distribution with density depression in the highly elongated central region which is surrounded by the region of maximum density (Fig. 32). Note that the SD configurations, which have the structure of ^{16}O + ^{16}O + two valence neutrons in molecular orbitals, have recently been predicted in the AMD + GCM calculations of Ref. [7].

The present study reveals also a number of other interesting molecular structures which are discussed below. We were able to trace some such configurations in an extended spin range

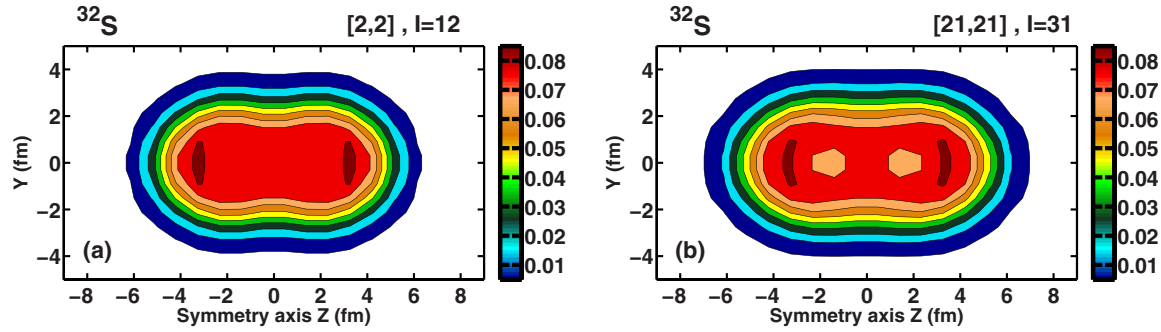

FIG. 29. The same as Fig. 8, but for ^{32}S.

starting from spin zero (or from very low spin), at which they are located at 20–30 MeV excitation energy above the ground state, up to very high spin where they are either yrast or close to the yrast line. These are the [42,31] and [42,22] MD configurations in ^{38}Ar (Fig. 25), the [31,31] and [41,41] MD configurations in ^{36}Ar (Fig. 22), the [42,42] MD configuration in ^{40}Ca (Fig. 1), the [62,42] MD configuration in ^{42}Ca (Fig. 13), the [62,62] MD configurations in ^{44}Ti (Fig. 16), and [52,52] and [421,421] MD configurations in ^{42}Sc (Fig. 10). These examples allowed us to study the impact of rotation on clusterization.

The molecular structures become well pronounced in the [31,31] and [41,41] MD configurations of ^{36}Ar [Figs. 24(c) and 24(d)], which are characterized by a well-established neck. They are also seen in the [42,31] configuration of ^{38}Ar [Figs. 33(a) and 33(b)]; note that in this case the rotation increases the separation of the fragments and makes the neck much more pronounced.

In ^{40}Ca, the density distribution of the MD [42,42] configuration at spin zero shows a triple-humped structure (top panel of Fig. 34). A similar configuration has been analyzed in Ref. [3] and it was concluded that α-cluster interpretation becomes quite fuzzy. Alternatively, one may consider this configuration as a ^{12}C + ^{16}O + ^{12}C chain built of distorted ^{16}O and ^{12}C nuclei. The validity of such interpretation should be verified in the future by comparison with the results of the cluster and/or AMD calculations similar to the ones presented in Ref. [3]. The comparison of the density distributions for this configurations at $I = 0\hbar$ and $I = 25\hbar$ (see Fig. 34) shows that the rotation hinders the tendency for clusterization. Indeed, the central hump becomes less pronounced and the depressions in the density distributions develop in central parts of the left and right segments at $I = 25\hbar$ (bottom panel of Fig. 34).

Similar effects are also seen in the MD [42,22] configuration of ^{38}Ar (see Fig. 7 in the Supplemental Material [78]), which could be considered as the MD [42,42] configuration of ^{40}Ca with two proton holes in the $N = 3$ orbitals. The addition of two neutrons to the MD [42,42] configuration of ^{40}Ca creates the MD [62,42] configuration in ^{42}Ca which has the features in the proton density distribution [see Figs. 33(c) and 33(d)] similar to the ones seen in Fig. 34.

These results show that in a few configurations discussed above the rotation tries to suppress the features of the density distribution that could be attributed to the clusterization. However, the density modifications induced by rotation definitely depend on the nucleonic configuration. For example, the density distribution of the [62,62] configuration in ^{48}Cr is

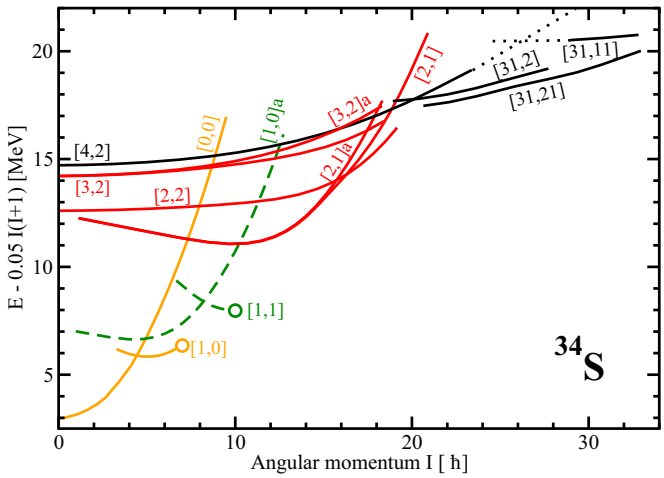

FIG. 30. The same as Fig. 1, but for ^{34}S.

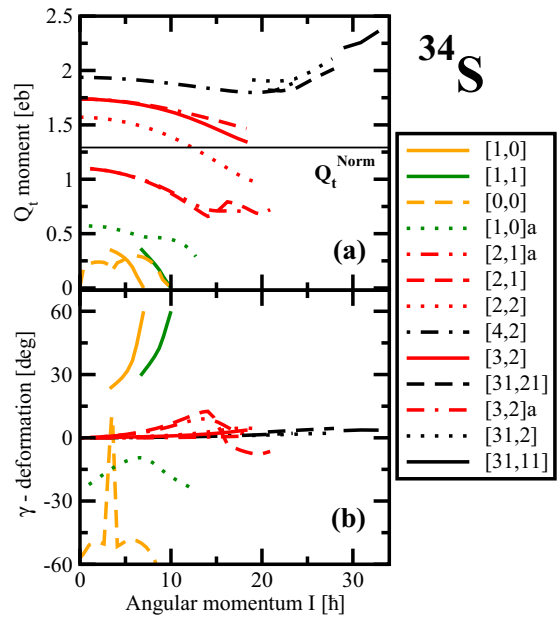

FIG. 31. The same as Fig. 5, but for ^{34}S.

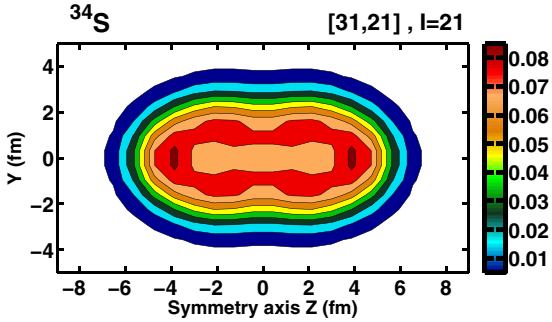

FIG. 32. The same as Fig. 8, but for ^{34}S.

modified only modestly by rotation [see Figs. 2(f) and 2(g) in the Supplemental Material [78]. Note that this configuration does not show the features typical for clusterization. However, with increasing spin the separation of the fragments becomes larger and the neck becomes more pronounced in the [42,31] configuration of ^{38}Ar [Figs. 33(a) and 33(b)] and the [421,421] configuration of ^{42}Sc [Figs. 12(c) and 12(d)].

Another interesting case of possible clusterization is the [62,62] MD configuration in ^{44}Ti [Figs. 33(e) and 33(f)]. Three fragments are clearly seen in the density distribution at $I = 0\hbar$, indicating a possible ^{16}O + ^{12}C + ^{16}O chain of nuclei. Note that with rotation the central fragment dissolves but two outer segments became slightly more pronounced. It is interesting that similar three fragments structure survives in the [52,52] MD configuration up to very high spins in ^{42}Sc [Fig. 12(b)]. This configuration could be considered as built from the [62,62] one in ^{44}Ti by creating proton and neutron holes in the $N = 3$ orbital.

A very interesting case of molecular structures is seen in the example of the [421,421] MD configuration in ^{42}Sc (Figs. 12(c) and 12(d) and and Fig. 1(a) in the Supplemental Material [78]). This system could probably be described as a combination of two prolate deformed ^{20}Ne cores located in tip-to-tip arrangement with extra proton and neutron.

It is necessary to understand that suggested interpretations of molecular structures are based on the consideration of only density distributions. Their validity should be verified in the future by the analysis of the wave functions of the

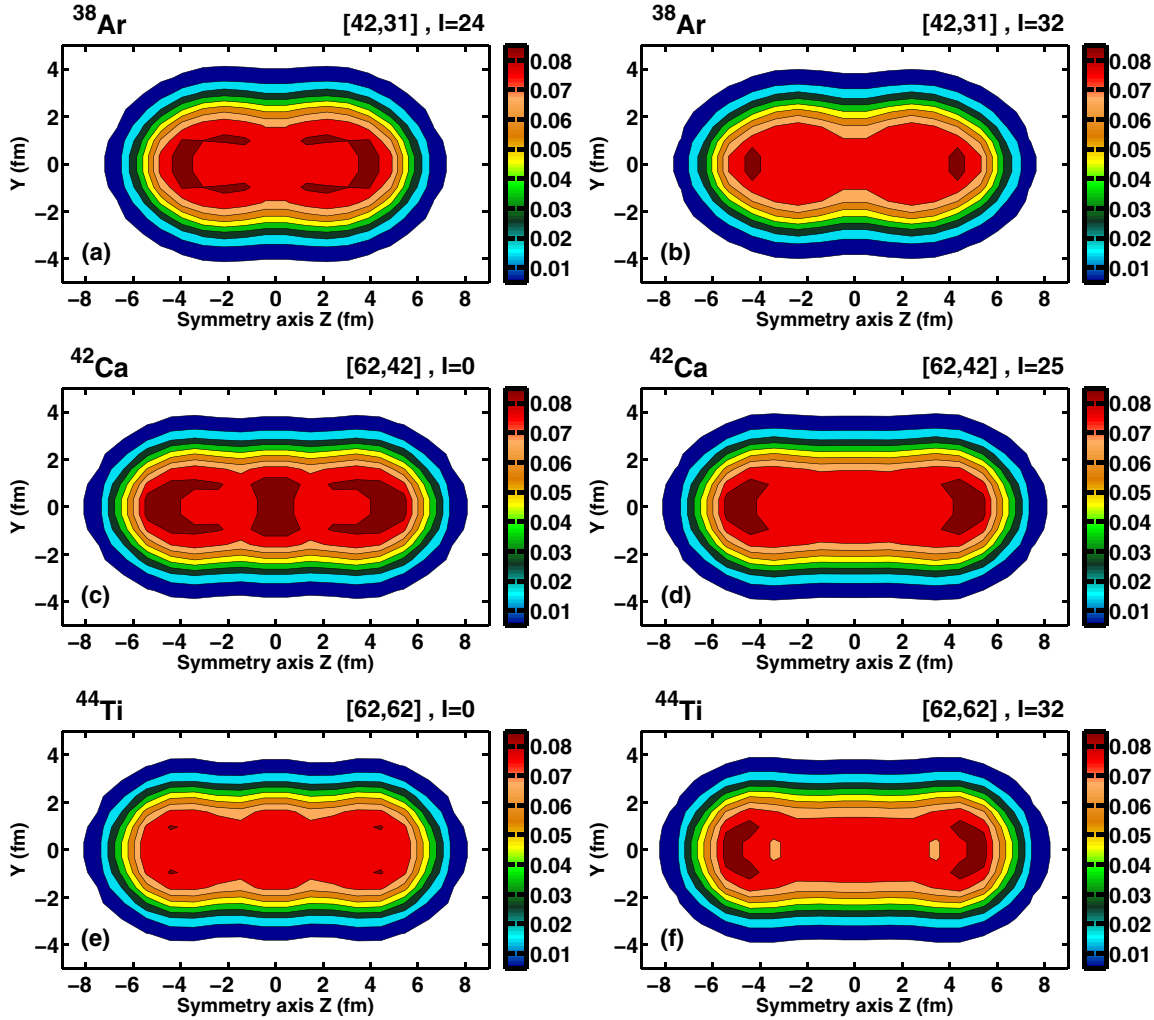

FIG. 33. The impact of rotation on the proton density distribution in selected configurations.

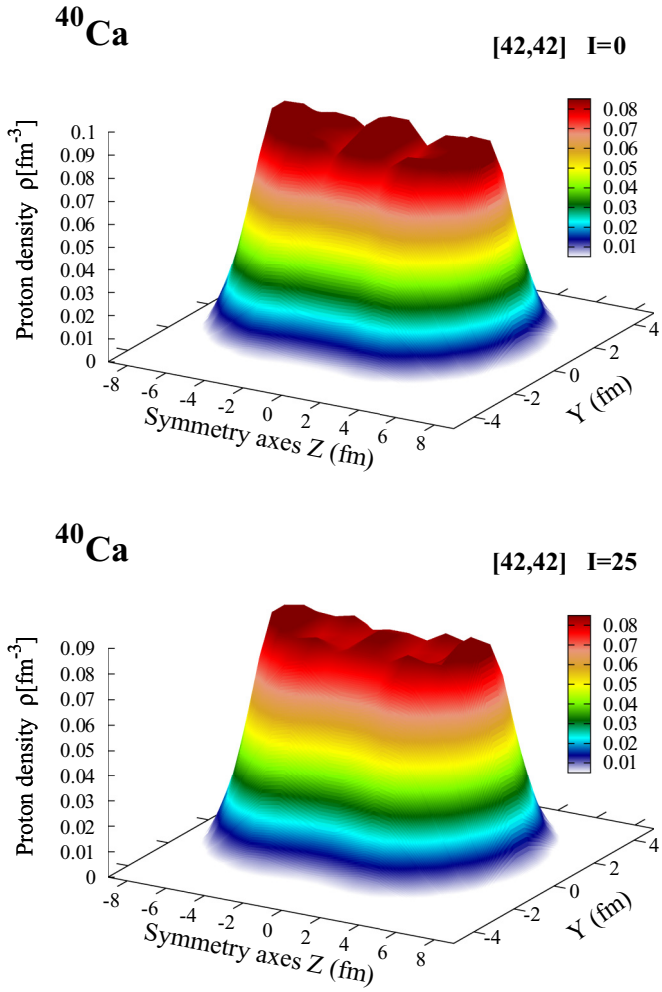

FIG. 34. Three-dimensional representation of the evolution or proton density distribution with spin in the [42,42] configuration of ^{40}Ca.

underlying configurations (and their overlaps with mean-field solutions) obtained in the cluster and/or antisymmetrized molecular dynamics calculations similar to the ones presented in Refs. [3,11].

VIII. ROTATIONAL PROPERTIES OF EXTREMELY DEFORMED CONFIGURATIONS

Most important physical observables characterizing the SD, HD, and MD structures are kinematic ($J^{(1)}$) and dynamic ($J^{(2)}$) moments of inertia and transition quadrupole moments Q_t. The latter provides direct information on the deformation of the charge distributions and that was a reason why the calculated Q_t values were presented earlier. It is, however, necessary to recognize that the previous history of the experimental investigation of the SD bands clearly shows that the Q_t quantity is measured in a dedicated experiment, and thus it is available only for a small fraction of the SD bands.

Thus, it is expected that in future experiments it will be easier to obtain the information on rotational properties of the bands which are described in terms of kinematic and dynamic moments of inertia using the expressions

$$J^{(1)}(\Omega_x) = J\left(\frac{dE}{dJ}\right)^{-1} = \frac{J}{\Omega_x}, \tag{3}$$

$$J^{(2)}(\Omega_x) = J\left(\frac{d^2E}{dJ^2}\right)^{-1} = \frac{dJ}{d\Omega_x}, \tag{4}$$

where

$$\Omega_x = \frac{dE}{dJ} \tag{5}$$

defines the rotational frequency and E and J are total energy and the expectation value of total angular momentum on the axis of rotation, respectively. Their experimental counterparts are extracted from the observed energies of the γ transitions within a band according to the prescription given in Sec. 4.1 of Ref. [20]. Note that the kinematic moment of inertia depends on the absolute values of spins, while only the differences $\Delta I = 2$ enter the definition of dynamic moment of inertia.

The SD bands observed in the $A \approx 40$ mass region are an exception from the general rule that the SD bands are very seldom linked to the low-spin level scheme. Thus, contrary to absolute majority of the SD bands in the nuclear chart their spins are known; it is quite likely that some SD bands which will be observed in this mass region in the future will follow this pattern. On the contrary, it is expected that the spins of the HD and MD bands will be difficult to define in future experiments. For such bands, only the dynamic moment of inertia will be available for comparison with the results of calculations.

The kinematic and dynamic moments of inertia of the (typically lowest in energy) SD, HD, and MD bands are presented in Fig. 35 for each nucleus under study. For a majority of the SD and HD bands one observes that the following condition $J^{(1)} \geqslant J^{(2)}$ is satisfied at medium and high frequencies. As discussed in Ref. [20] this condition is valid for the rotational bands in the unpaired regime. This condition is not valid in the region of unpaired band crossing with weak interaction, where $J^{(2)}$ grows rapidly with increasing rotational frequency. This takes place at the highest calculated frequencies in the [2,2] SD configuration of ^{32}S [Fig. 35(a)], [4,4] SD configuration in ^{40}Ca [Fig. 35(e)], and [62,62] HD configuration in ^{48}Cr [Fig. 35(k)]. Note also that such a situation is seen at medium spin in the [31,21] HD configuration of ^{34}S [Fig. 35(b)] and the [51,4] SD configuration of ^{44}Ca [Fig. 35(g)].

The moments of inertia of the MD bands show three different patterns of behavior. Some of the MD bands undergo a centrifugal stretching that results in an increase of the transition quadrupole moments Q_t with increasing rotational frequency. This process also reveals itself in the moments of inertia: The kinematic moments of inertia are either nearly constant or slightly increase with increasing rotational frequency, whereas the dynamic moments of inertia show two patterns of behavior. In one of them the dynamic moment of inertia is almost the same as the kinematic one at low to medium rotational frequencies, but then $J^{(2)}$ becomes bigger than $J^{(1)}$ and the difference between them gradually increases with frequency. These are the MD configurations shown in Figs. 35(e), 35(f),

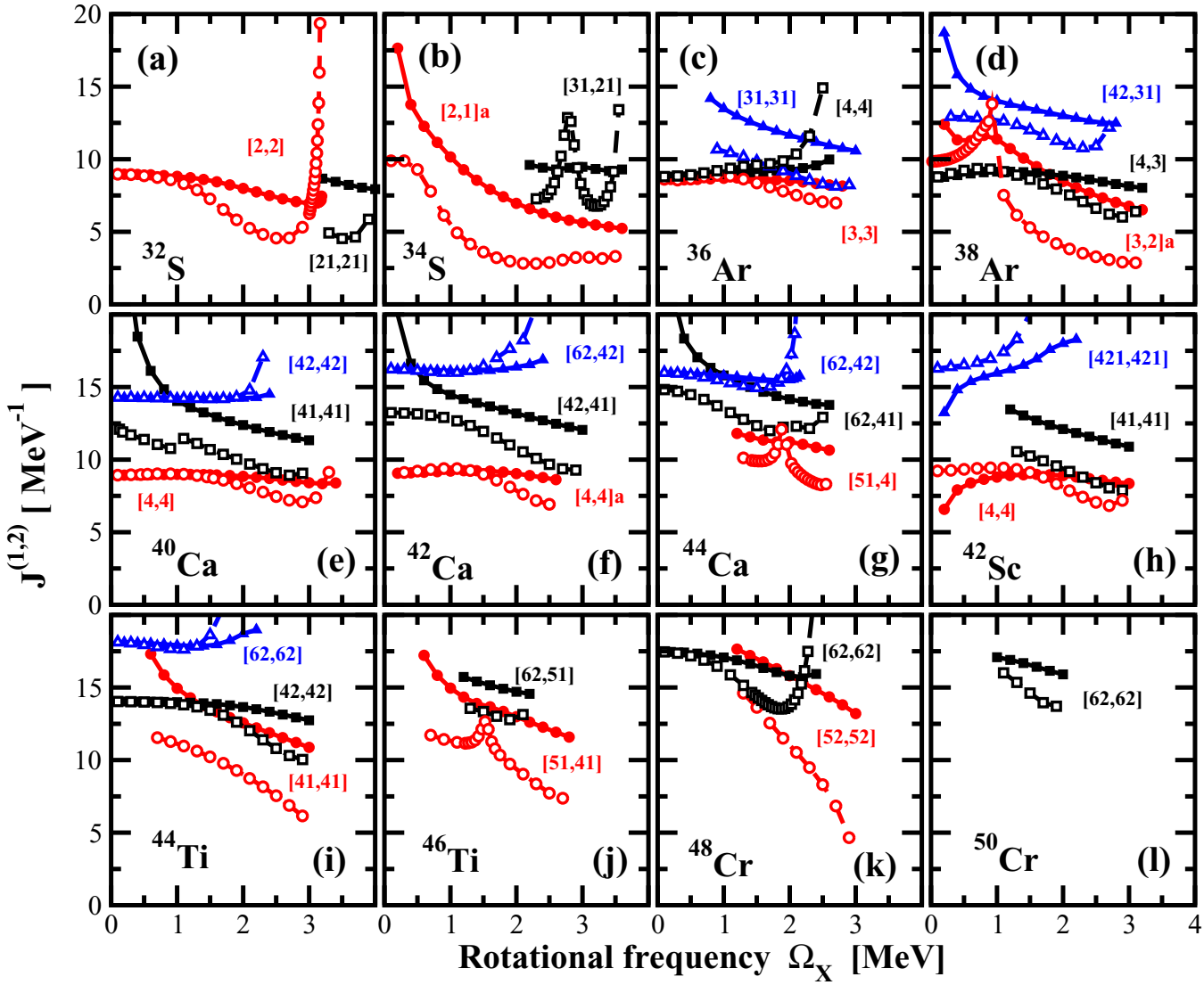

FIG. 35. Kinematic ($J^{(1)}$) and dynamic ($J^{(2)}$) moments of inertia of typical SD, HD, and MD configurations in indicated nuclei. The calculated $J^{(1)}$ and $J^{(2)}$ values are shown by solid and open symbols, respectively. Red circles, black squares, and blue triangles are used for the SD, HD, and MD configurations, respectively.

35(g), and 35(i). The pattern of the behavior of the [421,421] MD configuration in ^{42}Sc is very different [Fig. 35(h)]; both moments increase with increasing rotational frequency, but $J^{(2)} \geqslant J^{(1)}$ at all calculated frequencies. Note that this configuration has the most elongated density distribution among those studied in the present paper with a clear indication of molecular structure (see Sec. III.) The rotational properties of the above-discussed MD bands are very similar to the HD ones in the $Z = 40$–58 mass region investigated in Refs. [19,74]. However, the [31,31] MD configuration in ^{36}Ar [Fig. 35(c)] and [42,31] MD configuration in ^{38}Ar [Fig. 35(d)] show the relative properties of the two moments similar to the ones seen in the majority of the SD and HD bands shown in Fig. 35.

The examples shown in Fig. 35 clearly indicate strong dependence of the calculated $J^{(1)}$ and $J^{(2)}$ values on the nucleonic configuration and frequency. In most of the cases, at medium and high rotational frequencies there is a correlation between the moments of inertia and deformation so that the moments of inertia increase with increasing deformation. However, there are exceptions from this observation. For example, the dynamic moments of inertia of the [4,4] SD and [41,41] HD configurations in ^{42}Sc are quite similar [see Fig. 35(h)], despite substantial difference in the transition quadrupole moments [see Fig. 11(a)]. Even a more striking example is the similarity of dynamic moments of inertia of the [3,3] SD and [31,31] MD configurations in ^{36}Ar [Fig. 35(c)]. Such similarities are also seen for the kinematic moments of inertia, as illustrated by the case of the [52,52] SD and [62,62] HD bands in ^{48}Cr [Fig. 35(k)]. Thus, the decision on the nature of the band (SD, HD, or MD) observed in experiment cannot be based solely on the measured values of dynamic or kinematic moments of inertia; only the measurement of the transition quadrupole moment can reveal the true nature of the band.

IX. CONCLUSIONS

A systematic search for extremely deformed structures in the $N \approx Z$, $A \approx 40$ nuclei has been performed for the first time in the framework of covariant density functional theory. The aim of this study was to define at which spins such structures become yrast and their properties and to find the configurations showing the fingerprints of clusterization and molecular structures. The main results can be summarized as follows:

(i) The present investigation shows that extremely deformed structures inevitably become yrast with increasing spin in the nuclei under study. This is because normal and highly deformed configurations forming the yrast line at low and medium spins have limited angular momentum content. The key question is at which spin the transition from terminating to extremely deformed configurations takes place. This is basically defined by the maximum spin that could be built in terminating configurations with a limited number of particle-hole excitations across the respective spherical shell gaps. This spin is quite limited for particle-hole excitations across the proton $Z = 20$ and neutron $N = 20$ spherical shell gaps. As a result, the nuclei most favored for the observation of extremely deformed structures are located in the vicinity of ^{36}Ar and ^{40}Ca. For example, present calculations suggest that in ^{36}Ar the increase of spin above the measured $I = 16\hbar$ state is only possible by the population of the hyperdeformed band. On the contrary, the configurations built on particle-hole excitations across the spherical $N = 28$ and $N = 28$ gaps, which bring a substantial amount of angular momentum, dominate the yrast line at medium spin (up to $I \approx 30\hbar$) in the Cr nuclei. As a result, only at higher spins do extremely deformed configurations become yrast.

(ii) Similar to previous studies in the medium-mass nuclei [19,74], present calculations indicate that the $N = Z$ nuclei are better candidates for the observation of extremely deformed structures than the nuclei that have an excess of neutrons over protons because the transition to extremely deformed structures takes place at lower spins.

(iii) The above-discussed consideration of the most favored candidates for experimental observation of extremely deformed structures is based on the spins at which they become yrast in model calculations. However, it is expected that experimental observations will also depend on employed combination(s) of the target(s) and projectile(s) and respective cross sections of the reactions. Taking this factor and related uncertainties into account, the $N = Z$ and $N = Z + 2$ S, Ar, Ca, and Ti isotopes should be considered as good candidates for experimental observation of extremely deformed structures. However, the experimental observation of such structures in the ^{48,50}Cr isotopes is clearly disfavored by the present analysis as compared with the above-mentioned $N = Z$ and $N = Z + 2$ isotopes.

(iv) The underlying single-particle structure of nucleonic configurations with specific nodal structure of the single-particle density distribution leads to a clusterization in the form of molecular structures. The calculations suggest that in some nuclei such structures are either yrast or close to yrast at high spin. Thus, their observation with the new generation of γ-tracking detectors such as GRETA and AGATA may be possible in the near future. The calculations with cluster and/or antisymmetrized molecular dynamics models are definitely needed to establish the weights of those clusters in the structure of total wave function.

(v) The impact of rotation on the density distribution and clusterization (molecular nature) depends sensitively on nucleonic configuration. The density distributions of some configurations are only weakly affected by rotation. The features typical for clusterization, which are present at zero spin, are washed away by rotation in other configurations. However, the clusterization is enhanced by rotation in some specific configurations; with increasing spin the separation of the fragments becomes larger and the neck becomes more pronounced.

(vi) There is a strong dependence of the calculated kinematic and dynamic moments of inertia on the configuration and frequency. In most of the cases the moments of inertia increase with increasing deformation at medium and high rotational frequencies. However, there are exceptions from this observation. As a result, the decision on the nature of the band (SD, HD, or MD) observed in experiment cannot be based solely on the measured values of dynamic or kinematic moments of inertia; only the measurement of transition quadrupole moments will reveal the true nature of the band.

ACKNOWLEDGMENT

This material is based upon work supported by the U.S. Department of Energy, Office of Science, Office of Nuclear Physics under Award No. DE-SC0013037.

[1] Y. Kanada-En'yo and M. Kimura, Superdeformation and clustering in ^{40}Ca studied with antisymmetrized molecular dynamics, Phys. Rev. C **72**, 064322 (2005).

[2] W. von Oertzen, M. Freer, and Y. Kanada-En'yo, Nuclear clusters and nuclear molecules, Phys. Rep. **432**, 43 (2006).

[3] J. A. Maruhn, M. Kimura, S. Schramm, P.-G. Reinhard, H. Horiuchi, and A. Tohsaki, α-cluster structure and exotic states

in a self-consistent model for light nuclei, Phys. Rev. C **74**, 044311 (2006).
[4] Y. Taniguchi, M. Kimura, Y. Kanada-En'yo, and H. Horiuchi, Clustering and triaxial deformations of ^{40}Ca, Phys. Rev. C **76**, 044317 (2007).
[5] P.-G. Reinhard, J. A. Maruhn, A. S. Umar, and V. E. Oberacker, Localization in light nuclei, Phys. Rev. C **83**, 034312 (2011).
[6] J.-P. Ebran, E. Khan, T. Nikšić, and D. Vretenar, How atomic nuclei cluster, Nature (London) **487**, 341 (2012).
[7] Y. Taniguchi, Properties of the predicted superdeformed band in ^{32}S, Phys. Rev. C **90**, 054308 (2014).
[8] P. W. Zhao, N. Itagaki, and J. Meng, Rod-shaped Nuclei at Extreme Spin and Isospin, Phys. Rev. Lett. **115**, 022501 (2015).
[9] Y. Iwata, T. Ichikawa, N. Itagaki, J. A. Maruhn, and T. Otsuka, Examination of the stability of a rod-shaped structure in ^{24}Mg, Phys. Rev. C **92**, 011303 (2015).
[10] D. Jenkins, Alpha clustering in nuclei: another form of shape coexistence?, J. Phys. G **43**, 024003 (2016).
[11] M. Kimura and H. Horiuchi, ^{16}O + ^{16}O molecular nature of the superdeformed band of ^{32}S and the evolution of the molecular structure, Phys. Rev. C **69**, 051304 (2004).
[12] J.-P. Ebran, E. Khan, T. Nikšić, and D. Vretenar, Density functional theory studies of cluster states in nuclei, Phys. Rev. C **90**, 054329 (2014).
[13] J. L. Egido and L. M. Robledo, A mean field view of some clustering phenomena in light and heavy nuclei, Nucl. Phys. A **738**, 31 (2004).
[14] J. M. Yao, N. Itagaki, and J. Meng, Searching for a 4α linear-chain structure in excited states of ^{16}O with covariant density functional theory, Phys. Rev. C **90**, 054307 (2014).
[15] P. Arumugam, B. K. Sharma, S. K. Patra, and R. K. Gupta, Relativistic mean field study of clustering in light nuclei, Phys. Rev. C **71**, 064308 (2005).
[16] T. Ichikawa, J. A. Maruhn, N. Itagaki, and S. Ohkubo, Linear Chain Structure of Four-α Clusters in ^{16}O, Phys. Rev. Lett. **107**, 112501 (2011).
[17] H. Morinaga, Interpretation of Some of the Excited States of 4n Self-Conjugate Nuclei, Phys. Rev. **101**, 254 (1956).
[18] F. Hoyle, On Nuclear Reactions Occuring in Very Hot STARS. I. The Synthesis of Elements from Carbon to Nickel, Astrophys. J. Suppl. **1**, 121 (1954).
[19] A. V. Afanasjev and H. Abusara, Hyperdeformation in the cranked relativistic mean field theory: The $Z = 40$–58 region of the nuclear chart, Phys. Rev. C **78**, 014315 (2008).
[20] A. V. Afanasjev, D. B. Fossan, G. J. Lane, and I. Ragnarsson, Termination of Rotational Bands: Disappearance of Quantum Many-body Collectivity, Phys. Rep. **322**, 1 (1999).
[21] J. Dudek, K. Pomorski, N. Schunck, and N. Dubray, Hyper-deformed and megadeformed nuclei: Lessons from the slow progress and emerging new strategies, Eur. Phys. J. A **20**, 15 (2004).
[22] E. Ideguchi, D. G. Sarantites, W. Reviol, A. V. Afanasjev, M. Devlin, C. Baktash, R. V. F. Janssens, D. Rudolph, A. Axelsson, M. P. Carpenter, A. Galindo-Uribarri, D. R. LaFosse, T. Lauritsen, F. Lerma, C. J. Lister, P. Reiter, D. Seweryniak, M. Weiszflog, and J. N. Wilson, Superdeformation in the Doubly Magic Nucleus $^{40}_{20}$Ca$_{20}$, Phys. Rev. Lett. **87**, 222501 (2001).
[23] J. Zhang and W. Rae, Systematics of 2-dimensional α-cluster configurations in 4N nuclei from 12C to 44Ti, Nucl. Phys. A **564**, 252 (1993).
[24] C. J. Chiara, E. Ideguchi, M. Devlin, D. R. LaFosse, F. Lerma, W. Reviol, S. K. Ryu, D. G. Sarantites, C. Baktash, A. Galindo-Uribarri, M. P. Carpenter, R. V. F. Janssens, T. Lauritsen, C. J. Lister, P. Reiter, D. Seweryniak, P. Fallon, A. Görgen, A. O. Macchiavelli, and D. Rudolph, Transition quadrupole moments in the superdeformed band of ^{40}Ca, Phys. Rev. C **67**, 041303 (2003).
[25] C. E. Svensson *et al.*, Superdeformation in the $N = Z$ Nucleus ^{36}Ar: Experimental, Deformed Mean Field, and Spherical Shell Model Descriptions, Phys. Rev. Lett. **85**, 2693 (2000).
[26] C. E. Svensson *et al.*, Lifetimes of superdeformed rotational states in ^{36}Ar, Phys. Rev. C **63**, 061301 (2001).
[27] A. Bisoi, M. S. Sarkar, S. Sarkar, S. Ray, M. R. Basu, D. Kanjilal, S. Nag, K. Selvakumar, A. Goswami, N. Madhavan, S. Muralithar, and R. K. Bhowmik, Superdeformation and α-cluster structure in ^{35}Cl, Phys. Rev. C **88**, 034303 (2013).
[28] E. Ideguchi, S. Ota, T. Morikawa, M. Oshima, M. Koizumi, Y. Toh, A. Kimura, H. Harada, K. Furutaka, S. Nakamura, F. Kitatani, Y. Hatsukawa, T. Shizuma, M. Sugawara, H. Miyatake, Y. X. Watanabe, Y. Hirayama, and M. Oi, Superdeformation in asymmetric N>Z nucleus ^{40}Ar, Phys. Lett. B **686**, 18 (2010).
[29] D. G. Jenkins, C. J. Lister, M. P. Carpenter, P. Chowdury, N. J. Hammond, R. V. F. Janssens, T. L. Khoo, T. Lauritsen, D. Seweryniak, T. Davinson, P. J. Woods, A. Jokinen, H. Penttila, F. Haas, and S. Courtin, Candidate superdeformed band in ^{28}Si, Phys. Rev. C **86**, 064308 (2012).
[30] A. Di Nitto, E. Vardaci, A. Brondi, G. La Rana, M. Cinausero, N. Gelli, R. Moro, P. N. Nadtochy, G. Prete, and A. Vanzanella, Clustering effects in ^{48}Cr composite nuclei produced via the ^{24}Mg + ^{24}Mg reaction, Phys. Rev. C **93**, 044602 (2016).
[31] P. Papka, C. Beck, F. Haas, V. Raugh, M. Rousseau, P. Bednarczyk, S. Courtin, O. Dorvaux, K. Eddahbi, J. Robin, A. Sánchez i Zafra, O. Stezowski, and A. Prévost, Cluster emission and extremely deformed shapes in the N=Z nucleus ^{48}Ti, Acta Phys. Pol. B **34**, 2343 (2003).
[32] C. J. Chiara *et al.*, Probing *sd-fp* cross-shell interactions via terminating configurations in ^{42,43}Sc, Phys. Rev. C **75**, 054305 (2007).
[33] A. Bisoi, M. S. Sarkar, S. Sarkar, S. Ray, D. Pramanik, R. Kshetri, S. Nag, K. Selvakumar, P. Singh, A. Goswami, S. Saha, J. Sethi, T. Trivedi, B. S. Naidu, R. Donthi, V. Nanal, and R. Palit, High spin spectroscopy in ^{34}Cl, Phys. Rev. C **89**, 024303 (2014).
[34] S. Aydin *et al.*, High-spin level structure of ^{35}S, Phys. Rev. C **89**, 014310 (2014).
[35] A. Bisoi, M. S. Sarkar, S. Sarkar, S. Ray, D. Pramanik, R. Kshetri, S. Nag, K. Selvakumar, P. Singh, A. Goswami, S. Saha, J. Sethi, T. Trivedi, B. S. Naidu, R. Donthi, V. Nanal, and R. Palit, Collective excitations in ^{33}S, Phys. Rev. C **90**, 024328 (2014).
[36] M. Bender, H. Flocard, and P. H. Heenen, Beyond-mean-field-model analysis of low-spin normal-deformed and superdeformed collective states of ^{32}S, ^{36}Ar, ^{38}Ar, and ^{40}Ca, Phys. Rev. C **68**, 044321 (2003).
[37] M. Yamagami and K. Matsuyanagi, High-spin yrast structure of ^{32}S suggested by symmetry-unrestricted, cranked Hartree-Fock calculations, Nucl. Phys. A **672**, 123 (2000).
[38] T. Inakura, S. Mizutori, M. Yamagami, and K. Matsuyanagi, Cranked Skyrme-Hartree-Fock calculation for superdeformed and hyperdeformed rotational bands in N=Z nuclei from ^{32}S to ^{48}Cr , Nucl. Phys. A **710**, 261 (2002).

[39] H. Molique, J. Dobaczewski, and J. Dudek, Superdeformed bands in ^{32}S and neighboring nuclei predicted within the Hartree-Fock method, Phys. Rev. C **61**, 044304 (2000).
[40] R. R. Rodríguez-Guzmán, J. L. Egido, and L. M. Robledo, Properties of the predicted superdeformed band in ^{32}S, Phys. Rev. C **62**, 054308 (2000).
[41] A. V. Afanasjev, P. Ring, and I. Ragnarsson, Mean field studies of high-spin properties in the $A \sim 30$ and 60 regions of superdeformation, *Proceedings of the International Workshop PINGST2000, 2000, Lund, Sweden*, edited by D. Rudolph and M. Hellström (Bloms i Lund AB, 2000), p. 183.
[42] Y. Taniguchi, Y. Kanada-En'yo, M. Kimura, K. Ikeda, H. Horiuchi, and E. Ideguchi, Triaxial superdeformation in ^{40}Ar, Phys. Rev. C **82**, 011302 (2010).
[43] D. Vretenar, A. V. Afanasjev, G. A. Lalazissis, and P. Ring, Relativistic Hartree-Bogoliubov Theory: Static and Dynamic Aspects of Exotic Nuclear Structure, Phys. Rep. **409**, 101 (2005).
[44] A. V. Afanasjev, Band terminations in density functional theory, Phys. Rev. C **78**, 054303 (2008).
[45] H. Flocard, P. H. Heenen, S. J. Krieger, and M. S. Weiss, From ground state to scission: the spinning life of ^{20}Ne, Nucl. Phys. A **391**, 285 (1982).
[46] W. Koepf and P. Ring, A relativistic description of rotating nuclei: the yrast line of ^{20}Ne, Nucl. Phys. A **493**, 61 (1989).
[47] A. V. Afanasjev and H. Abusara, Time-odd mean fields in covariant density functional theory: Rotating systems, Phys. Rev. C **82**, 034329 (2010).
[48] E. Caurier, J. L. Egido, G. Martínez-Pinedo, A. Poves, J. Retamosa, L. M. Robledo, and A. P. Zuker, Intrinsic vs Laboratory Frame Description of the Deformed Nucleus ^{48}Cr, Phys. Rev. Lett. **75**, 2466 (1995).
[49] B. D. Serot and J. D. Walecka, Recent progress in quantum hadrodynamics, Adv. Nucl. Phys. **16**, 1 (1986).
[50] P.-G. Reinhard, The relativistic mean-field description of nuclei and nuclear dynamics, Rep. Prog. Phys. **52**, 439 (1989).
[51] J. König and P. Ring, Identical bands in superdeformed nuclei: A relativistic description, Phys. Rev. Lett. **71**, 3079 (1993).
[52] A. V. Afanasjev, J. König, and P. Ring, Superdeformed rotational bands in the $A \sim 140-150$ mass region: A cranked relativistic mean field description, Nucl. Phys. A **608**, 107 (1996).
[53] A. V. Afanasjev and S. Frauendorf, Description of rotating $N = Z$ nuclei in terms of isovector pairing, Phys. Rev. C **71**, 064318 (2005).
[54] A. V. Afanasjev, I. Ragnarsson, and P. Ring, Comparative study of superdeformed and highly deformed bands in the $A \sim 60$ mass region, Phys. Rev. C **59**, 3166 (1999).
[55] A. V. Afanasjev, Y. Shi, and W. Nazarewicz, Description of ^{158}Er at ultrahigh spin in nuclear density functional theory, Phys. Rev. C **86**, 031304(R) (2012).
[56] A. V. Afanasjev, Rotating nuclei: from ground states to the extremes of spin and deformation, *Relativistic Density Functional for Nuclear Structure*, International Review of Nuclear Physics, Vol. 10, edited by J. Meng (World Scientific Publishing Co. Pte. Ltd., Singapore, 2016), pp. 305–354.
[57] A. V. Afanasjev and O. Abdurazakov, Pairing and rotational properties of actinides and superheavy nuclei in covariant density functional theory, Phys. Rev. C **88**, 014320 (2013).
[58] A. V. Afanasjev and H. Abusara, Time-odd mean fields in covariant density functional theory: nonrotating systems, Phys. Rev. C **81**, 014309 (2010).
[59] A. V. Afanasjev and P. Ring, Time-odd mean fields in the rotating frame: Microscopic nature of nuclear magnetism, Phys. Rev. C **62**, 031302(R) (2000).
[60] P. Ring and P. Schuck, *The Nuclear Many-Body Problem* (Springer-Verlag, Berlin, 1980).
[61] M. J. A. de Voigt, J. Dudek, and Z. Szymański, High-spin phenomena in atomic nuclei, Rev. Mod. Phys. **55**, 949 (1983).
[62] Y. R. Shimizu, J. D. Garrett, R. A. Broglia, M. Gallardo, and E. Vigezzi, Pairing fluctuations in rapidly rotating nuclei, Rev. Mod. Phys. **61**, 131 (1989).
[63] A. V. Afanasjev, P. Ring, and J. König, Cranked relativistic Hartree-Bogoliubov theory: formalism and application to the superdeformed bands in the $A \sim 190$ region, Nucl. Phys. A **676**, 196 (2000).
[64] J. Dobaczewski, A. V. Afanasjev, M. Bender, L. M. Robledo, and Y. Shi, Properties of nuclei in the nobelium region studied within the covariant, Skyrme, and Gogny energy density functionals, Nucl. Phys. A **944**, 388 (2015).
[65] G. A. Lalazissis, S. Karatzikos, R. Fossion, D. P. Arteaga, A. V. Afanasjev, and P. Ring, The effective force NL3 revisited, Phys. Lett. B **671**, 36 (2009).
[66] S. E. Agbemava, A. V. Afanasjev, D. Ray, and P. Ring, Global performance of covariant energy density functionals: Ground state observables of even-even nuclei and the estimate of theoretical uncertainties, Phys. Rev. C **89**, 054320 (2014).
[67] A. V. Afanasjev and S. Shawaqfeh, Deformed one-quasiparticle states in covariant density functional theory, Phys. Lett. B **706**, 177 (2011).
[68] H. Abusara, A. V. Afanasjev, and P. Ring, Fission barriers in actinides in covariant density functional theory: the role of triaxiality, Phys. Rev. C **82**, 044303 (2010).
[69] A. V. Afanasjev, T. L. Khoo, S. Frauendorf, G. A. Lalazissis, and I. Ahmad, Cranked relativistic Hartree-Bogoliubov theory: Probing the gateway to superheavy nuclei, Phys. Rev. C **67**, 024309 (2003).
[70] S. Hilaire and M. Girod, Large-scale mean-field calculations from proton to neutron drip lines using the D1S Gogny force, Eur. Phys. J. **33**, 237 (2007).
[71] M. Samyn, S. Goriely, and J. M. Pearson, Further explorations of Skyrme-Hartree-Fock-Bogoliubov mass formulas. V. Extension to fission barriers, Phys. Rev. C **72**, 044316 (2005).
[72] W. Nazarewicz and I. Ragnarsson, Nuclear deformations, in *Handbook on Nuclear Properties*, edited by D. N. Poenaru and W. Greiner (Claredon Press, Oxford, 1996), p. 80.
[73] E. Caurier, J. Menéndez, F. Nowacki, and A. Poves, Coexistence of spherical states with deformed and superdeformed bands in doubly magic ^{40}Ca: A shell-model challenge, Phys. Rev. C **75**, 054317 (2007).
[74] H. Abusara and A. V. Afanasjev, Hyperdeformation in the Cd isotopes: A microscopic analysis, Phys. Rev. C **79**, 024317 (2009).
[75] C. Andreoiu *et al.*, High-spin lifetime measurements in the $N = Z$ nucleus ^{72}Kr, Phys. Rev. C **75**, 041301 (2007).
[76] C. D. O'Leary, C. E. Svensson, S. G. Frauendorf, A. V. Afanasjev, D. E. Appelbe, R. A. E. Austin, G. C. Ball, J. A. Cameron, R. M. Clark, M. Cromaz, P. Fallon, D. F. Hodgson, N. S. Kelsall, A. O. Macchiavelli, I. Ragnarsson, D. Sarantites, J. C. Waddington, and R. Wadsworth, Evidence for isovector neutron-proton pairing from high-spin states in $N = Z$ ^{74}Rb, Phys. Rev. C **67**, 021301(R) (2003).

[77] F. Brandolini, S. Lenzi, D. Napoli, R. Ribas, H. Somacal, C. Ur, D. Bazzacco, J. Cameron, G. de Angelis, M. D. Poli, C. Fahlander, A. Gadea, S. Lunardi, G. Martinez-Pinedo, N. Medina, C. R. Alvarez, J. Sanchez-Solano, and C. Svensson, Precise DSAM lifetime measurements in ^{48}Cr and ^{50}Cr as a test of large scale shell model calculations, Nucl. Phys. A **642**, 387 (1998).

[78] See Supplemental Material at http://link.aps.org/supplemental/10.1103/PhysRevC.94.014310 for the results of the calculations not included in the main body of the paper.

[79] E. Caurier, F. Nowacki, and A. Poves, Shell Model Description of the Decay Out of the Superdeformed Band of ^{36}Ar, Phys. Rev. Lett. **95**, 042502 (2005).

[80] R. Sheline, I. Ragnarsson, and S. Nilsson, Shell structure for deformed nuclear shapes, Phys. Lett. B **41**, 115 (1972).

[81] G. Leander and S. Larsson, Potential-energy surfaces for the doubly even $N = Z$ nuclei, Nucl. Phys. A **239**, 93 (1975).

[82] T. Tanaka, R. G. Nazmitdinov, and K. Iwasawa, Nonaxial octupole deformations in light $N = Z$ nuclei at high spins, Phys. Rev. C **63**, 034309 (2001).